https://lib.uliege.be https://matheo.uliege.be

Continuous Wavelet Transform Analysis of Mesoscale Motions Contribution to Scalar Transport at the ICOS Sites of Lonzée and Vielsalm.

Auteur : Hac, Guillaume
Promoteur(s) : Heinesch, Bernard; Charles, Catherine
Faculté : Gembloux Agro-Bio Tech (GxABT)
Diplôme : Master en bioingénieur : sciences et technologies de l'environnement, à finalité spécialisée
Année académique : 2024-2025
URI/URL : http://hdl.handle.net/2268.2/24354

Avertissement à l'attention des usagers :

Tous les documents placés en accès ouvert sur le site le site MatheO sont protégés par le droit d'auteur. Conformément aux principes énoncés par la "Budapest Open Access Initiative"(BOAI, 2002), l'utilisateur du site peut lire, télécharger, copier, transmettre, imprimer, chercher ou faire un lien vers le texte intégral de ces documents, les disséquer pour les indexer, s'en servir de données pour un logiciel, ou s'en servir à toute autre fin légale (ou prévue par la réglementation relative au droit d'auteur). Toute utilisation du document à des fins commerciales est strictement interdite.

Par ailleurs, l'utilisateur s'engage à respecter les droits moraux de l'auteur, principalement le droit à l'intégrité de l'oeuvre et le droit de paternité et ce dans toute utilisation que l'utilisateur entreprend. Ainsi, à titre d'exemple, lorsqu'il reproduira un document par extrait ou dans son intégralité, l'utilisateur citera de manière complète les sources telles que mentionnées ci-dessus. Toute utilisation non explicitement autorisée ci-avant (telle que par exemple, la modification du document ou son résumé) nécessite l'autorisation préalable et expresse des auteurs ou de leurs ayants droit.

CONTINUOUS WAVELET TRANSFORM ANALYSIS OF MESOSCALE MOTIONS CONTRIBUTION TO SCALAR TRANSPORT AT THE ICOS SITES OF LONZÉE AND VIELSALM

GUILLAUME HAC

THESIS SUBMITTED IN VIEW OF OBTAINING THE DEGREE OF MASTER IN
BIOENGINEERING SPECIALIZED IN ENVIRONMENTAL SCIENCES AND TECHNOLOGIES

ACADEMIC YEAR 2024–2025

Supervisors: Pr. HEINESCH Bernard & Pr. CHARLES Catherine
Advisor: BITTON Jonathan

CONTINUOUS WAVELET TRANSFORM ANALYSIS OF MESOSCALE MOTIONS CONTRIBUTION TO SCALAR TRANSPORT AT THE ICOS SITES OF LONZÉE AND VIELSALM

GUILLAUME HAC

THESIS SUBMITTED IN VIEW OF OBTAINING THE DEGREE OF MASTER IN BIOENGINEERING SPECIALIZED IN ENVIRONMENTAL SCIENCES AND TECHNOLOGIES

ACADEMIC YEAR 2024–2025

Supervisors: Pr. HEINESCH Bernard & Pr. CHARLES Catherine
Advisor: BITTON Jonathan

Remerciements - Acknowledgments

Je souhaite adresser mes remerciements à toutes celles et ceux qui ont apporté leur aide ou leur soutien au cours de ce travail. Je tiens notamment à remercier mes promoteurs, Bernard Heinesch et Catherine Charles, pour l’attention qu’ils ont portée à ce projet, la confiance qu’ils m’ont accordée, ainsi que pour la rigueur et la clarté de leurs remarques, qui m’ont permis de garder le cap dans ce travail.

Je tiens à exprimer ma gratitude à Jonathan Bitton, qui m’a d’abord offert l’opportunité de m’intégrer à son travail et qui m’a par la suite accompagné tout au long de ce mémoire avec beaucoup de calme et de pédagogie.

Je souhaite également remercier ma sœur, Olivia, pour son soutien et sa présence, qui m’ont été d’une grande aide dans la phase finale de ce mémoire.

Par ailleurs, ce travail a été rendu possible grâce à la mise en œuvre de la transformée en ondelettes par Jonathan Bitton et à la méthode de calcul du ratio de bilan énergétique (EBR) développée par Néo Arquin. Les ressources de calcul ont été mises à disposition par le Consortium des Équipements de Calcul Intensif (CÉCI), financé par le Fonds de la Recherche Scientifique de Belgique (F.R.S.-FNRS) sous la convention n° 2.5020.11, ainsi que par la Région wallonne.

Abstract

The eddy covariance (EC) method is the standard approach for quantifying turbulent exchanges of energy and carbon dioxide (CO_2) between ecosystems and the atmosphere, yet its application reveals a systematic lack of energy balance closure (EBC). A leading hypothesis for this observation is the unaccounted contribution from mesoscale motions, characterized by eddies with timescales exceeding the conventional 30-minute averaging window of EC. This study investigates the role of such motions through the application of the wavelet transform (WT), a method that allows time–frequency analysis of single-point tower-based measurements.

High-frequency measurements from the complete 2020 datasets at two ICOS sites in Belgium, a cropland in Lonzée and a mixed forest in Vielsalm, were analyzed. Fluxes of sensible heat (H), latent heat (LE), and CO_2 (FC) estimated with the WT were compared to EC across different scales. At both sites, EC indicated systematic underestimation of turbulent fluxes, with annual energy balance ratios (EBR) of 0.65 in Lonzée and 0.73 in Vielsalm. Wavelet-derived fluxes tended to underestimate microscale contributions relative to EC, especially in the case of LE in Lonzée, but revealed additional mesoscale components. These contributions were negligible at Lonzée ($< 2\%$) but averaged 5% of the microscale fluxes at Vielsalm, improving the EBR when included. In addition, the mesoscale component of FC followed the trends of the energy fluxes, although a decoupling becomes apparent under higher temperature conditions ($> 16°$C).

The results highlight the role of site characteristics, including measurement height, canopy height, topography, and meteorological conditions, in determining the magnitude of mesoscale transport.

Résumé

La méthode d’eddy covariance (EC) constitue l’approche de référence pour quantifier les échanges turbulents d’énergie et de dioxyde de carbone (CO_2) entre les écosystèmes et l’atmosphère. Toutefois, son application révèle un déficit systématique de fermeture du bilan d’énergie (EBC). Une hypothèse majeure avancée pour expliquer cette observation est la contribution non prise en compte des mouvements de mésoéchelle, caractérisés par des tourbillons dont l’échelle de temps dépasse la fenêtre conventionnelle de moyennage de 30 minutes utilisée en EC. Cette étude examine le rôle de ces mouvements au moyen de la transformée en ondelettes (WT), une méthode qui permet une analyse temps–fréquence à partir de mesures en un seul point sur des tours micrométéorologiques.

Des mesures à haute fréquence couvrant l’ensemble de l’année 2020 ont été analysées sur deux sites ICOS en Belgique : une parcelle agricole à Lonzée et une forêt mixte à Vielsalm. Les flux de chaleur sensible (H), de chaleur latente (LE) et de CO_2 (FC) estimés par WT ont été comparés à ceux obtenus par EC à différentes échelles. Sur les deux sites, l’EC a montré une sous-estimation systématique des flux turbulents, avec des rapports annuels de bilan d’énergie (EBR) de 0.65 à Lonzée et de 0.73 à Vielsalm. Les flux issus de la WT ont tendance à sous-estimer les contributions de petite échelle par rapport à l’EC, en particulier pour LE à Lonzée, mais ont permis de mettre en évidence des composantes supplémentaires de mésoéchelle. Ces contributions se sont révélées négligeables à Lonzée ($< 2\%$), mais représentaient en moyenne 5% des flux de petite échelle à Vielsalm, améliorant l’EBR lorsqu’elles étaient prises en compte. De plus, la composante de mésoéchelle de FC suit globalement les tendances des flux d’énergie, bien qu’un découplage devienne apparent sous des conditions de température plus élevées ($>$ 16°C).

Les résultats mettent en évidence le rôle des caractéristiques de site, incluant la hauteur de mesure, la hauteur de la canopée, la topographie et les conditions météorologiques, dans la détermination de l’ampleur du transport de mésoéchelle.

Contents

List of Abbreviations

Abbreviation	**Meaning**
ABL	Atmospheric Boundary Layer
CO_2	Carbon Dioxide
CWT	Continuous Wavelet Transform
EBC	Energy Balance Closure
EBR	Energy Balance Ratio
EC	Eddy Covariance
FC	Carbon Flux
H	Sensible Heat Flux
ICOS	Integrated Carbon Observation System
LE	Latent Heat Flux
LES	Large Eddy Simulation
NEE	Net Ecosystem Exchange
R_{net}	Net radiation
PBL	Planetary Boundary Layer
WT	Wavelet Transform
XWT	Cross Wavelet Transform
u^*	Friction Velocity
z/L	Monin–Obukhov Stability Parameter
ρ_{air}	Air density
c_p	Specific heat capacity of air at constant pressure
L_v	Latent heat of vaporization
M_{H_2O}	Molar mass of water vapor
M_{air}	Molar mass of dry air
ρ_{mol}	Molar density of air
w	Wind speed
m	Metre
χ	Water vapor mixing ratio

1 Introduction

Micrometeorology is the branch of meteorology dedicated to studying the lowest layer of the atmosphere, the atmospheric boundary layer (ABL), where direct exchanges of heat, moisture, momentum and gases occur between the surface and the air above. This layer is directly influenced by the Earth's surface. Solar heating warms the ground and causes large parcels of air to rise, while cooler, denser air aloft tends to sink. These vertical motions generate large eddies, while frictional drag at the surface and differential wind speeds with height induce wind shear, breaking larger eddies into smaller ones. This process, in which smaller eddies draw energy from larger ones, is called the energy cascade (Stull, 1988). Ultimately, the smallest eddies dissipate their energy as heat through molecular viscosity. Phenomena in this layer typically occur on spatial scales smaller than one or two kilometers and on timescales shorter than a day (Stull, 1988). Turbulent motions in the ABL regulate the transfer of energy and matter, influencing key ecosystem processes such as evapotranspiration and carbon exchange (Patton et al., 2016). Eddies smaller than 3 km and with timescales shorter than one hour are usually classified as microscale (Stull, 1988), though other classifications exist (Foken & Nappo, 2008). In the present work, microscale refers to eddies with timescales shorter than 30 minutes and mesoscale to eddies between 30 minutes and one day. The size of eddies can also be inferred from their frequencies using Taylor's hypothesis of frozen turbulence, valid when their timescale exceeds the time it takes for them to advect past the sensor (Stull, 1988).

As climate change has become one of the main concerns of modern society, understanding how ecosystems respond to varying environmental conditions is essential to sustain agricultural and forest production (Baldocchi, 2003). Numerous ”greener” practices have been theorized, implemented, and even financially supported. However, ecosystems are inherently complex. For example, attempts to sequester carbon in soils can sometimes have unintended consequences, such as triggering the priming effect, which can lead to a net release of carbon dioxide (CO_2) instead of its storage (Bastida et al., 2019; Bernard et al., 2022). Another example of counteracting feedback emerges from permafrost regions under climate warming. Rising temperatures enhance microbial respiration, promoting CO_2 emissions through the decomposition of previously frozen organic matter. At the same time, increased nitrogen availability from permafrost thaw stimulates vegetation growth and Net Primary Production (NPP), potentially offsetting some of the carbon losses through enhanced sequestration (Liu et al., 2024).

Advancing our understanding of ecosystem–atmosphere interactions requires continuous monitoring of the exchanges occurring at their interface. While concentrations of CO_2 and water vapor have been measured since the 1950s, it is only in recent years that technological advancements have made it possible to continuously measure surface–atmosphere fluxes across multiple sites (Baldocchi et al., 2001). It is in light of these challenges that, in 1998, the National Aeronautics and Space Administration (NASA) launched the FLUXNET project. Its purpose is to coordinate, process, and distribute data collected from around the globe (Baldocchi et al., 2001). In Europe, the Integrated Carbon Observation System (ICOS) contributes to this global effort as a research infrastructure providing standardized, long-term observations of greenhouse gas exchanges from the atmosphere, terrestrial ecosystems, and the ocean (Franz et al., 2018). Due to the inherently chaotic nature of turbulence, a deterministic description of eddies is nearly impossible. As a result, micrometeorologists rely on statistical approaches to characterize turbulent motions. In this framework, and under the assumption that during the day turbulence is the main means of scalar transport near the surface, the variance of vertical wind speed represents the intensity of turbulence, while covariances between vertical wind speed and scalars quantify their transport (Stull, 1988). Since the 1990s, the eddy covariance (EC) method has become the standard method for observing surface–atmosphere exchanges across a wide range of biomes and climatic zones (Aubinet et al., 2012; Baldocchi et al., 2001). This method allows direct measurement at the canopy scale (Baldocchi, 2003) by computing the covariance between the vertical wind speed (w) and the scalar quantity of interest, such as temperature (T), water mixing ratio (χ), or CO_2 mixing ratio (c).

However, applying statistical tools in this context requires the assumption of the ergodic hypothesis, which states that time averages are equivalent to ensemble averages (Kaimal & Finnigan, 1994). Hence, the fluctuations have to be statistically stationary during the averaging time (Aubinet et al., 2012; Foken & Wichura, 1996). In other words, without stationarity, the measured averages cannot reliably capture the actual behavior of the turbulence over the observed period. Furthermore, for the measurement to be representative, a homogeneous surface is assumed (Foken & Wichura, 1996). The choice of an averaging period was made in relation to the spectral gap (see Figure 1) as it appears to be a gap in the occurrence of eddies of a period ranging from 30 minutes to several hours (Stull, 1988). This gap serves as a separation between turbulent-scale and synoptic-scale motions. The presence of a spectral gap justifies the choice of the averaging period (Destouet et al., 2024). However, the condition of stationarity is not always met in practice, as factors such as topography, land cover heterogeneity, and even transient effects such as differential cloud shadowing (Letzel & Raasch, 2003) can introduce spatial and temporal gradients on surface properties. The invalidity of the condition introduces systematic errors in the estimations (Foken & Wichura, 1996; Liu et al., 2022; Mahrt, 1998; Vitale et al., 2020). To ensure the validity of statistical assumptions, half-hour periods that fail to meet the stationarity criterion are commonly excluded from the analysis, resulting in data gaps where fluxes cannot be reliably estimated (Aubinet et al., 2012).

To evaluate the accuracy of the EC measurements, one common approach is to assess the energy balance closure (EBC) (Wilson et al., 2002). The idea is to consider the system closed and to compare the turbulent energy to any other sink and source. This leads to the following budget equation :

$$R_{\text{net}} = H + LE + G + S + \varepsilon \tag{1}$$

Where R_{net} is the net radiation, H and LE are the sensible (H) and latent heat fluxes (LE), respectively, S represents the heat storage within the canopy air space and biomass, G is the ground heat flux by conduction, and ϵ denotes the residual term associated with potential measurement errors and unaccounted processes. Even when accounting for the possible range of error of instrumentation for R_{net} and the uncertainty of G and S, it remains clear that the turbulent fluxes are systematically underestimated (Aubinet, 2012; Twine et al., 2000; Foken, 2008; Baldocchi, 2003). This lack of energy closure, in turn, raises questions concerning the CO_2 fluxes (FC) estimation (Twine et al., 2000). Moreover, the correlation between the imbalance of energy fluxes and FC might be complex, especially when the influencing factor of the different fluxes differs (Zhou et al., 2024).

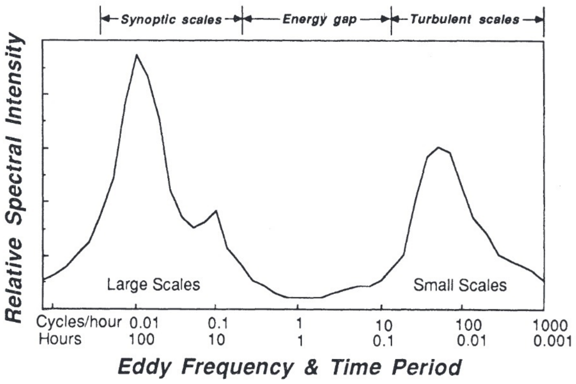

Figure 1: Schematic spectrum of wind speed near the ground. Adapted from Stull (1988).

Several reasons for this lack of balance closure were hypothesized by Mauder (2020), including (i) systematic measurement errors, (ii) neglected storage terms, (iii) advection due to landscape heterogeneity and (iv) the missed contribution of mesoscale motions. As is often the case, heat storage within plant biomass is usually ignored because its direct measurement would require deploying numerous temperature sensors on various parts of the canopy (Gu et al., 2007). To circumvent the effects of localised heterogeneity, tower-based measurements are sometimes paired with aircraft measurements as an attempt to scale up data acquired from one point tower measurements (Desjardins et al., 1995; Etling and Brown, 1993; Mauder et al., 2007). However, such campaigns are costly and typically limited to short durations (Loescher et al., 2006). The focus of the present study is to investigate the last factor, namely the missing mesoscale contribution. This factor is directly linked to the fact that the EC method inherently acts as a high pass filter (Mauder et al., 2020; Finnigan et al., 2002), meaning that any contribution from motions with timescales of over 30 minutes would not be accounted for. These motions are likely to emerge from heterogeneity in the landscape (Panin et al., 1998; Patton et al., 2005; Stoy et al., 2013; Mauder and Foken, 2006; Inagaki et al., 2006; Vidale et al., 1997; Finnigan et al., 2003). For example, differences in soil moisture can influence turbulence structure (Zhang et al., 2011), as can thermal contrasts at the surface (Letzel & Raasch, 2003) and complex topography (Turnipseed et al., 2004). The presence of mesoscales circulation would induce non-stationarity as their contribution would be interpreted as advection if mesoscale motions move past the point of measurement (Panin et al., 1998) or as a mean vertical velocity (which should be equal to zero for EC assumption to hold) (Aubinet et al., 2012) if a stationary thermal is present as illustrated in Figure 2. (Patton et al., 2005; Lee and Black, 1993). The consequences would therefore be a violation of both the ergodicity assumption and Taylor's frozen turbulence hypothesis (Mauder et al., 2020). This explains why the idea of detrending signals to ensure stationarity was abandoned, as it would effectively filter out contributions from mesoscale motions (Mahrt, 1998) and therefore, lead to systematic errors.

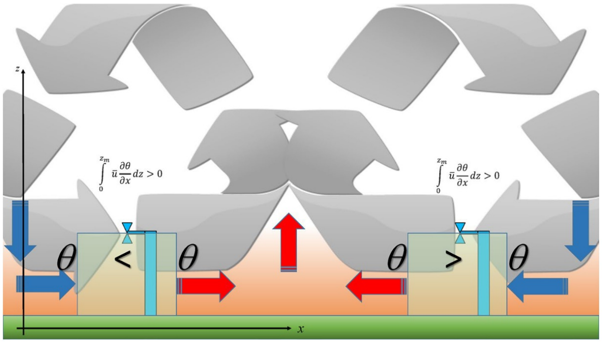

Figure 2: Bias in tower-based EC flux measurements caused by large-scale organized structures in the ABL. Red and blue arrows indicate upward and downward motions transporting heat and water vapor. Blue boxes mark the virtual control volumes around the towers. Adapted from Mauder (2020).

Given these constraints, a method has been proposed by several authors to quantify the contribution of mesoscale motions directly from existing tower measurements (Mauder et al., 2007; Terradellas et al., 2001; Farge, 1992). The Wavelet Transform (WT) is a mathematical tool used in signal processing that enables the simultaneous analysis of signals in both the time and scale domains. Originally developed by Morlet in the early 1980s for seismic signal analysis, the wavelet transform was later formalized by Grossmann and Morlet (1984) and refined by Daubechies (1990). Initially applied in fields such as image processing (Liu, 1994) and later in oceanography (Fan et al., 2019), it was introduced into micrometeorology in the 1990s through studies by Collineau and Brunet (1993a,b) on coherent structures in forest canopies, and by Katul and Vidakovic (1996) on turbulence energy partitioning. Wavelet-based methods have since been used to examine mesoscale contribution to turbulent fluxes and EBC (Collineau & Brunet, 1993a,b; Katul & Vidakovic, 1996; Thomas & Foken, 2005; Mauder et al., 2007), showing that a significant part of the flux can occur at scales beyond the conventionally assumed spectral gap.

A key advantage of the WT is that it does not require stationarity (Daubechies, 1990), which allows for the extension of the averaging period beyond the typical limitations of the EC method. While EC acts as a high-pass filter (Mauder et al., 2020; Finnigan et al., 2002), the WT functions as a band-pass filter (Torrence & Compo, 1998), enabling the independent quantification of the contribution of each scale of eddies to the transport of any scalar. The WT provides time–scale coefficients, from which variances and covariances at each scale can be obtained by averaging over time (Kumar & Foufoula-Georgiou, 1997). The objective of this study is to further explore the contribution of mesoscale motions to the EBC by means of the WT. Specifically, it aims to investigate this closure at two ICOS sites located in Belgium, a mixed forest in Vielsalm and a cropland in Lonzée, originally addressed by Tzvetkov (2023). Expanding the size of the dataset to a full year, this work addresses the following questions:

- How do EC and WT flux estimates compare when evaluated over the same scales?
- To what extent do previously overlooked low-frequency motions contribute to H, LE and FC?
- Does accounting for these contributions improve the EBC?
- Under which environmental conditions are these contributions enhanced?
- How are these contributions reflected in FC?

The next section presents the two study sites and the datasets used. It then outlines the theoretical foundations of the EC method and introduces the metric employed in this work to evaluate the EBC, namely the energy balance ratio (EBR). This is followed by a description of the WT and its associated tools and concludes with the methodological steps applied.

2 Materials and Methods

This section presents the methodology and tools used in this work. It begins with a description of the study sites, followed by an overview of the theoretical foundations of EC, and a brief explanation of how the EBR is calculated. The next part covers the WT, outlining its theoretical background and its application to the analysis of turbulent fluxes, along with the specific parameterizations applied in this study. Finally, the procedure used for data processing and the computation of the WT is described.

2.1 Sites description

The data used in this study were collected from two ICOS-labelled stations in Belgium, Lonzée and Vielsalm. Both sites operate under ICOS standard protocols and use the EC method to quantify turbulent exchanges of heat, water vapor, and CO_2 between the surface and the atmosphere. The regional climate is classified as temperate oceanic (Cfb, Köppen classification), with moderate temperatures and precipitations distributed throughout the year (ICOS, 2020), and both sites experience predominantly southwesterly winds. Measurements of water vapor and CO_2 mixing ratios are obtained using an enclosed-path infrared gas analyzer (LI-COR LI-7200). Wind components and sonic temperature are measured with a three-dimensional sonic anemometer (Gill HS-50). The measurements are recorded at a sampling frequency of 20 Hz.

Lonzée

The first site is a cropland located in Lonzée, at an elevation of 167 meters above sea level. The size of the parcel is approximately 400 m x 400 m (Tzvetkov , 2023). The target area is composed of a flat agricultural field with no significant surrounding obstructions. The site follows a four-year crop rotation consisting of sugar beet (*Beta vulgaris L.*), winter wheat (*Triticum aestivum L.*), potato (*Solanum tuberosum L.*), and again winter wheat (*Triticum aestivum L.*). The terrain is essentially flat, with no relevant slope, and is classified as silty loam. According to the ICOS labelling report, the site meets the criteria of the footprint representativeness test defined by Kljun et al. (2015), ensuring adequate spatial coverage of the target area by the measured fluxes. The measurement instruments are mounted on a fixed mast at 2.06 meters above ground level.

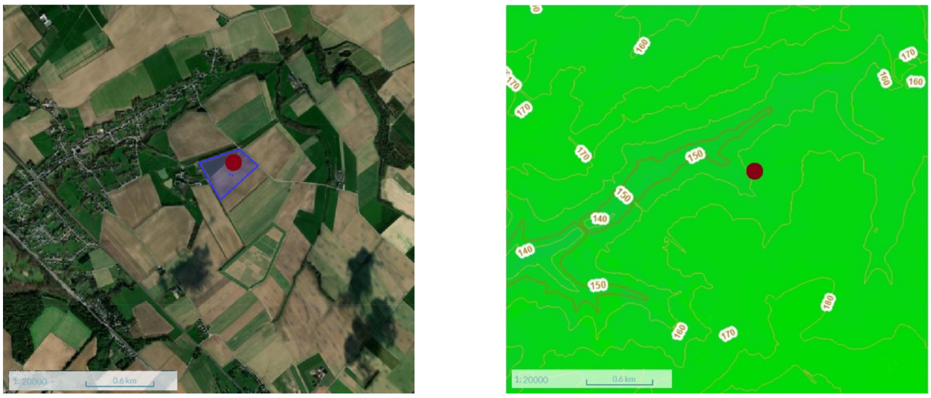

(a) (b)

Figure 3: View of the Lonzée site: (a) satellite image with the target area, (b) topographic map.

Vielsalm

The second site is a mixed forest located in Vielsalm, at 490 meters above sea level. The target area is more heterogeneous than in Lonzée, as it encompasses ten different tree species. The forest is mainly composed of Douglas fir (*Pseudotsuga menziesii*), European beech (*Fagus sylvatica L.*), European silver fir (*Abies alba Mill.*) and Norway spruce (*Picea abies (L.) H.Karst.*). The canopy height was measured at 34.6 meters in 2014 and the terrain has an average slope of 3% (Aubinet et al., 2001). The soil is classified as a loamy soil. Flux measurements are performed at a height of 51 meters, ensuring that the sensors are above the canopy. The site also passes the ICOS footprint representativeness test.

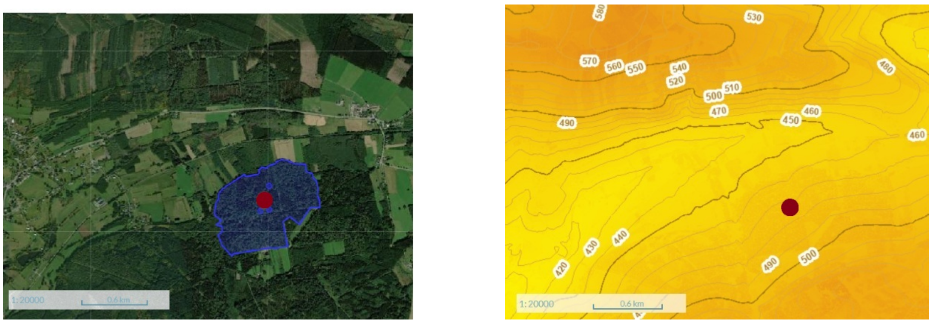

(a) (b)

Figure 4: View of the Vielsalm site: (a) satellite image with the target area, (b) topographic map.

2.2 The eddy covariance method

The EC method allows the direct estimation of turbulent fluxes of mass or energy, such as heat, water vapor, and trace gases, between the land surface and the atmosphere (Aubinet et al., 1999). It relies on high-frequency measurements of vertical wind speed and of the scalar concentrations above the canopy. The theoretical foundation of the EC method lies in the scalar conservation equation, which expresses the rate of change over time of a scalar quantity 'c' in the atmosphere.

At one point, the scalar budget can be written as :

$$\frac{\partial c}{\partial t} + \nabla \cdot (c\mathbf{u}) = S + D \tag{2}$$

Where c is the scalar of interest, u, v, and w are the wind-velocity components along the direction of the mean (x), the lateral (y) and vertical (z) wind. S is the source/sink term, and D corresponds to molecular diffusion. In most EC applications, molecular diffusion is negligible compared with turbulent transport as it is only relevant within the first few centimeters above the surface (Stull, 1988).

Because our interest is at the ecosystem scale, Equation (2) is integrated over a volume of control V above the surface (Figure 5). After expanding the divergence, the term $c\left(\frac{\partial u}{\partial x} + \frac{\partial v}{\partial y} + \frac{\partial w}{\partial z}\right)$ cancels out by applying the continuity equation for incompressible flow ($\nabla \cdot \mathbf{u} = 0$). Integrating over V leads to :

$$\int_V \left[\frac{\partial c}{\partial t} + u\frac{\partial c}{\partial x} + v\frac{\partial c}{\partial y} + w\frac{\partial c}{\partial z}\right] dV = \int_V S\, dV \tag{3}$$

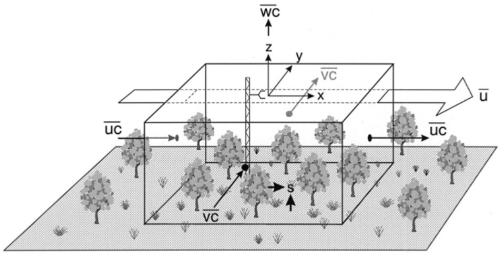

Figure 5: Schematic illustration of flux integration over a control volume. Adapted from Aubinet (2012).

To characterise turbulent flow, each measured variable is expressed as the sum of two components: a mean value and a fluctuating term. This procedure, known as Reynolds decomposition, is only valid under the hypothesis of ergodicity. This assumption requires the process to remain statistically stationary over the averaging period, with stable mean and variance. If this condition is not met, the decomposition loses its validity and the resulting flux estimates may be biased (Foken & Wichura, 1996). Further details on the application of the Reynolds decomposition are available in Appendix 1. Its application to variables in Equation (3) is written as $c = \overline{c} + c'$, $u = \overline{u} + u'$, $v = \overline{v} + v'$, $w = \overline{w} + w'$. Where the overbar denotes the average over a chosen time window, the standard averaging period being 30 minutes for EC, and the prime denotes the instantaneous deviation from that mean. Applying this decomposition to the scalar conservation equation leads to Equation (4).

$$\int_V \left[\frac{\partial \overline{c}}{\partial t} + \left(\overline{u}\frac{\partial \overline{c}}{\partial x} + \frac{\partial(\overline{u'c'})}{\partial x}\right) + \left(\overline{v}\frac{\partial \overline{c}}{\partial y} + \frac{\partial(\overline{v'c'})}{\partial y}\right) + \left(\overline{w}\frac{\partial \overline{c}}{\partial z} + \frac{\partial(\overline{w'c'})}{\partial z}\right)\right] dV = \int_V \overline{S}\, dV \quad (4)$$

By rearranging terms in Equation (4) :

$$\int_V \left[\underbrace{\frac{\partial \overline{c}}{\partial t}}_{\text{I}} + \underbrace{\left(\overline{u}\,\frac{\partial \overline{c}}{\partial x} + \overline{v}\,\frac{\partial \overline{c}}{\partial y}\right)}_{\text{II}} + \underbrace{\overline{w}\,\frac{\partial \overline{c}}{\partial z}}_{\text{III}} + \underbrace{\left(\frac{\partial\,\overline{u'c'}}{\partial x} + \frac{\partial\,\overline{v'c'}}{\partial y}\right)}_{\text{IV}} + \underbrace{\frac{\partial\,\overline{w'c'}}{\partial z}}_{\text{V}}\right] dV \;=\; \underbrace{\int_V \overline{S}\, dV}_{\text{VI}} \quad (5)$$

Where Term I is the storage and quantifies how the mean scalar in the control volume changes with time. Term II is the mean horizontal advection, describing scalar transport by the average wind along the x and y directions. Term III is the mean vertical advection, quantifying the scalar transport by the mean vertical wind. Term IV is the horizontal divergence of the turbulent flux, capturing how the turbulent transport varies laterally. Term V is the vertical divergence of the turbulent flux that expresses how the turbulent transport of c varies with height. Finally, Term VI is the source/sink term, corresponding to the production and consumption of the scalar by the ecosystem.

Equation (5) can be simplified as a result of certain hypotheses. In the case where the flow is stationary over the averaging window, Term I can be approximated as zero. This simplification is valid for long-term estimations since the daily mean of this term is zero, but can become significant over shorter periods of time and for tall canopies (Aubinet et al., 1999). If the surface is flat and horizontally homogeneous, Terms II and IV can be considered negligible (Baldocchi, 2003). This assumption greatly simplifies practical estimation, since otherwise the fluxes would need to be measured at multiple locations along the horizontal axes to account for their gradients in the x and y directions. Finally, over low crops and close to the surface, the mean vertical wind is typically near zero, making Term III practically negligible. However, this assumption is not valid over tall canopies, when measurements are made at greater heights (Lee, 1998).

The hypothesis of horizontal homogeneity also allows for a simplification of the spatial integration. If horizontal gradients are negligible, the point of measurement becomes representative of the volume in the x and y directions, the integration is reduced to the vertical direction (Aubinet, 2012), with h being the height of the measurement point and the budget can be expressed per unit area :

$$\int_0^h \frac{\partial \overline{c}}{\partial t}\, dz + \int_0^h \frac{\partial \overline{w'c'}}{\partial z}\, dz = \int_0^h \overline{S}\, dz \quad (6)$$

By applying the vertical integration to the second term of the equation and assuming a vertical profile for this term :

$$\int_0^h \frac{\partial \overline{c}}{\partial t}\, dz + \overline{w'c'}\bigg|_{z=h} - \overline{w'c'}\bigg|_{z=0} = \int_0^h \overline{S}\, dz \tag{7}$$

If we assume that there is no turbulent flux at ground level $\overline{w'c'}\bigg|_{z=0} = 0$, the final equation becomes :

$$\int_0^h \frac{\partial \overline{c}}{\partial t}\, dz + \overline{w'c'}\bigg|_{z=h} = \int_0^h \overline{S}\, dz \tag{8}$$

The covariance between vertical wind fluctuations w' and scalar fluctuations c at the measurement height h defines the turbulent flux of c. It quantifies the net vertical transport of c by eddies. In the generalized EC framework, the total ecosystem-atmosphere exchange of the scalar is obtained by combining this turbulent flux and the storage term (Aubinet, 2012).

2.3 EBR

The EBR is a commonly used metric to assess the degree of closure of the surface energy balance in EC measurements. It is defined as the ratio between the sum of turbulent fluxes of H and LE and the available energy, calculated as R_{net} minus G and S :

$$EBR = \frac{H + LE}{R_{\text{net}} - G - S} \tag{9}$$

In ideal conditions, the EBR should equal unity, reflecting a perfect closure of the energy balance. However, numerous field studies have reported systematic underestimations of turbulent fluxes, resulting in EBR values typically ranging from 0.7 to 0.95 (Wilson et al., 2002; Foken, 2008a; Mauder & Foken, 2020). The lack of closure has been attributed to several factors, including mesoscale transport (Mauder & Foken, 2020), horizontal and vertical advection (Aubinet et al., 2012), heat storage in biomass (Meyers, 2004), measurement uncertainties (Loescher et al., 2006), and data processing procedures (Mauder & Foken, 2006).

In this study, the S includes contribution from the air column under the point of measurement for H and LE, the soil heat storage in the upper 5 cm as well as the energy associated with the photosynthetic processes in relation to FC, but does not account for heat storage within the biomass. The EBR can be computed over different time scales, ranging from half-hourly to seasonal or annual periods, depending on the objectives of the analysis. In this study, EBR values are computed at the half-hourly scale. As indicated in Equation (9), the EBR can become highly unstable when R_{net} approaches zero. However, in this case, such conditions are unlikely since the present analysis will be restricted to daytime periods.

Another metric used is the energy imbalance (Foken, 2008), which is expressed as :

$$\text{Imbalance} = (R_{\text{net}} - G - S) - (H + LE) \tag{10}$$

While the EBR is a relative, dimensionless measure of closure, the imbalance expresses the absolute difference between available energy and turbulent fluxes in W m^{-2}. The imbalance is often described as the total contribution of neglected processes and uncertainties (Mauder, 2020).

2.4 The wavelet transform

As presented during the theoretical foundations of EC, the method relies on assumptions such as stationarity and fixed averaging periods. These constraints limit its ability to capture low-frequency motions and to assess how different temporal scales contribute to the observed flux imbalance. To overcome these limitations, the WT provides a complementary framework for flux analysis. The WT is a mathematical tool used in signal processing for spectral analysis. It relies on the same theoretical foundations as the Fourier transform (FT), but unlike the FT, which assumes signal stationarity and provides only frequency-domain information, the WT allows the spectral analysis of non-stationary time series while preserving the temporal localization of frequencies (Torrence & Compo, 1998). The main difference lies in the choice of the analyzing function: while the FT uses infinite harmonic sinusoids, the WT uses short-lived oscillations that are limited in time. These “small waves” gave the method its name, derived from the French word *ondelettes*.

General formula

The general formula of the Continuous Wavelet Transform (CWT) is written as :

$$T_x(a,b) = \int_{-\infty}^{+\infty} x(t)\, \psi^*_{a,b}(t)\, dt \tag{11}$$

Where $T_x(a,b)$ is the wavelet coefficient at scale a and time b, $x(t)$ is the time series under analysis, $\psi^*_{a,b}(t)$ represents the mother wavelet $\psi(t)$ scaled and translated by the parameters a and b, and the asterisk denotes the complex conjugate.

This formulation corresponds to the definition of a scalar product in the Hilbert space $L^2(\mathbb{R})$ between the signal and a scaled–translated version of the mother wavelet. The coefficient $T_x(a,b)$ therefore expresses the degree of similarity between the analyzed signal and the wavelet at the chosen scale and time (Bitton, 2019). Figure 6 shows a geometric interpretation of the coefficient.

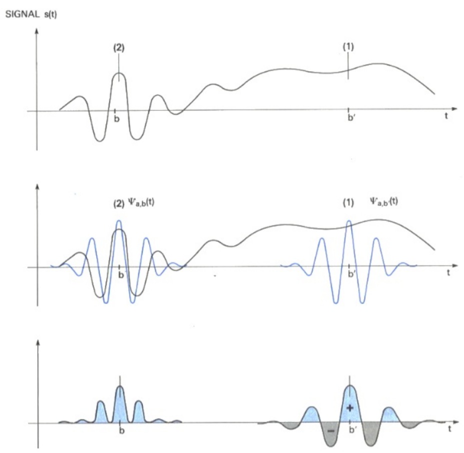

Figure 6: Geometric interpretation of the wavelet coefficient $C_{a,b}$ for (1) an irregular signal and (2) a constant signal, showing the resulting integration area. Adapted from Bitton (2019), after Meyer et al. (1987).

Mother wavelet

A mother wavelet is the original function from which all analyzing wavelets are derived through scaling and translation. To be admissible, a mother wavelet must satisfy two main conditions.

The first condition is:

$$C_\psi = 2\pi \int_0^{+\infty} \frac{|\Psi(\omega)|^2}{|\omega|} \, d\omega < +\infty \tag{12}$$

Where C_ψ is the admissibility constant of the mother wavelet and ω is the angular frequency. This condition ensures that the wavelet transform preserves the original signal's energy and that the latter can be reconstructed from its wavelet coefficients (Bitton, 2019). It also guarantees that the signal's total variance can be decomposed across scales and subsequently reconstructed by integrating the wavelet variance over the entire scale range (Kumar & Foufoula-Georgiou, 1994). This preservation of information is essential for obtaining variance, and thus covariance values, that can be reliably converted into real fluxes in physical units.

The second condition, which stems from the first, is that its mean must be zero, ensuring the absence of a zero-frequency component :

$$\Psi(0) = \int_{-\infty}^{+\infty} \psi(t) \, dt = 0 \tag{13}$$

Where $\Psi(0)$ is the Fourier transform of the mother wavelet $\psi(t)$. This property allows the wavelet to capture only variations in the signal while filtering out its constant part.

The wavelet selected for this study is the complex Morlet wavelet (Figure 7), which has both real and imaginary components. Its mathematical expression is given by :

$$\psi(t) = e^{-j\omega_0 t} e^{-\frac{t^2}{2}} \tag{14}$$

,

and can be viewed as a sinusoidal function modulated by a Gaussian bell curve.

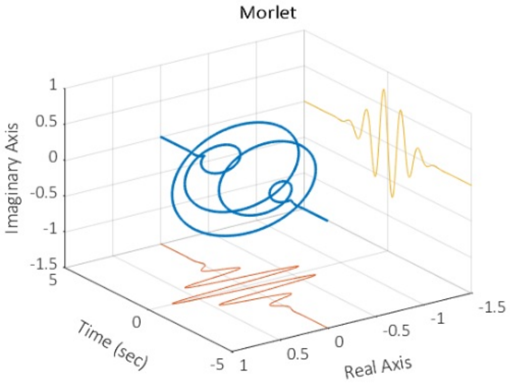

Figure 7: Representation of the Morlet wavelet. Adapted from Bitton (2019).

This mathematical expression makes use of Euler's identity $e^{jy} = \cos(y) + j\sin(y)$ to express the sinusoidal part of the wavelet as a complex exponential. The Morlet wavelet does not strictly satisfy the first admissibility condition, but for $\omega_0 > 5$, $\psi(0)$ becomes negligible, and ω_0 is therefore fixed to 6 in this study. Here, ω_0 refers to the dimensionless frequency (Torrence & Compo, 1998) which controls the number of oscillations contained within the Gaussian envelope. The sinusoidal structure of this wavelet makes it particularly suitable for analyzing wave-like phenomena (Terradellas et al., 2001) and provides good resolution in the frequency domain (Thomas & Foken, 2005). The Morlet wavelet is a continuous, smooth oscillation, which makes it an appropriate choice for signals with gradual amplitude variations (Torrence & Compo, 1998). This is the case for variables such as scalar concentrations and wind speed, where turbulent eddies of different sizes are dynamically related through the energy cascade.

Daughter wavelet

The functions derived from the mother wavelet are referred to as daughter wavelets and their relationship to the mother wavelet is given by :

$$\psi_{a,b}(t) = \lambda_{\text{norm}}\, \psi\left(\frac{t-b}{a}\right) \tag{15}$$

The scaling parameter a controls the dilation or compression of the wavelet, which determines the range of frequencies analyzed. It does not directly correspond to the frequency, but rather stretches or contracts the entire wavelet. This choice reflects the time–frequency compromise inherent in spectral analysis, conceptually linked to the Heisenberg uncertainty principle, which implies that achieving finer resolution in time necessarily comes at the expense of resolution in the frequency domain, and vice versa (Bitton, 2019). The wavelet transform addresses this dilemma by adapting the resolution depending on the scale (Farge, 1992). At lower frequencies, the wavelet is dilated, reducing its resolution in the time domain but improving its resolution in the frequency domain. Conceptually, for slow phenomena that occur over a long period, precise localization in time is less important, while frequency resolution becomes more relevant, and the opposite holds for fast, short-lived events.

The translation parameter b shifts the wavelet along the time axis, allowing it to be compared with different parts of the signal.

And finally, λ_{norm} is a normalizing factor. Two normalization conventions are generally adopted (Bitton, 2019):

- The L^1 norm, for which $\|\psi_{a,b}(t)\| = \|\psi(t)\|$, which preserves the amplitude between the daughter and mother wavelet.
- The L^2 norm, for which $\|\psi_{a,b}(t)\|^2 = \|\psi(t)\|^2$, which preserves the energy between the daughter and mother wavelet.

The set of scales, which determines the range of sizes of the daughter wavelets, must be chosen to cover the desired range of frequencies to be analyzed. In this study, the set of scales was chosen following the approach proposed by Torrence and Compo (1998) and is defined as:

$$a_j = a_0\, 2^{j\delta j}, \qquad j = 0, 1, 2, \ldots, J$$

$$J = \frac{1}{\delta j}\,\log_2\!\left(\frac{a_{\max}}{a_0}\right)$$

Where a_0 and $a_{\max}$ are the minimum and maximum scales analyzed, respectively. Between these two limits, the scales are defined using logarithmic spacing controlled by δ_j, which determines the sampling density in the frequency domain. The scale evolution is logarithmic in order to cover a broader spectrum of eddy sizes. For the Morlet wavelet, the relationship between the wavelet scale a_j and its corresponding oscillation period, referred to as the “Fourier period” λ_j, follows the formulation given in Bitton (2019) :

$$\lambda_j = \frac{2\pi}{\omega_0} a_j \tag{16}$$

Scalogram

In this study, the analyzed signals are represented as 2D graphs, with one dimension representing time and the other the scalar value of a given variable, such as vertical wind speed, temperature, χ or CO_2 mixing ratio. When the WT is applied, the result is a two-dimensional output matrix with one axis for time and the other for frequency (or period). Each wavelet coefficient has an associated magnitude, the square of which is proportional to the variance of the signal at the corresponding time and scale. The graphical representation of this matrix is called a scalogram, and Figure 8 shows a simple example taken from Bitton (2019).

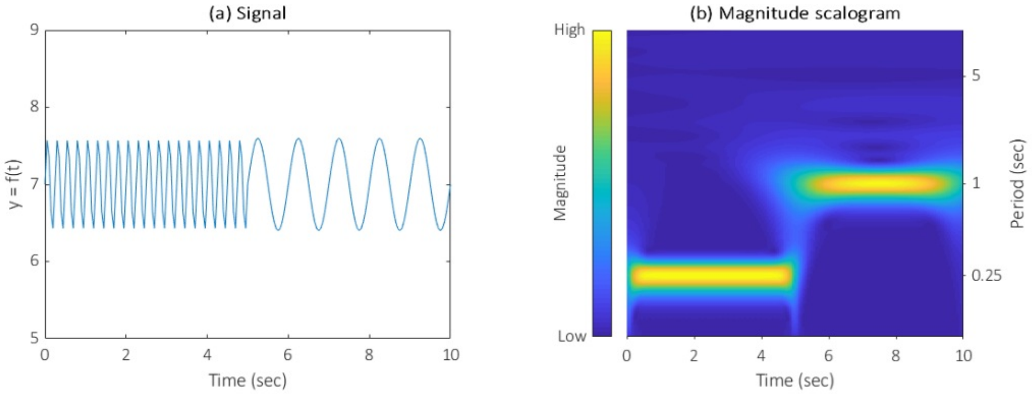

Figure 8: (a) Representation of a synthetic signal composed of two periodic components with periods of 0.25 and 1 s, respectively, and (b) the associated scalogram obtained using the Morlet wavelet. Adapted from Bitton (2019).

Cone of influence

The time series on which the WT is performed are finite. This implies that the signal is surrounded at both ends by regions without data. The border of the region in the wavelet coefficient matrix where the results of the WT are significantly influenced by those edge effects is called the cone of influence (COI) (Torrence & Compo, 1998). The wavelet coefficients outside of the COI border are omitted.

Kirby and Swain (2013) define the width of the COI for a given wavelet as the distance in the time domain from its maximum amplitude to the point where its envelope has decreased to q_{coi} of that maximum with $q_{coi} < 1$. In practice, one method consists of generating a Dirac impulse at both ends of the signal and their COI defines the region over which the value of the wavelet coefficient is considered unreliable for analysis as presented in Figure 9 (Bitton, 2019).

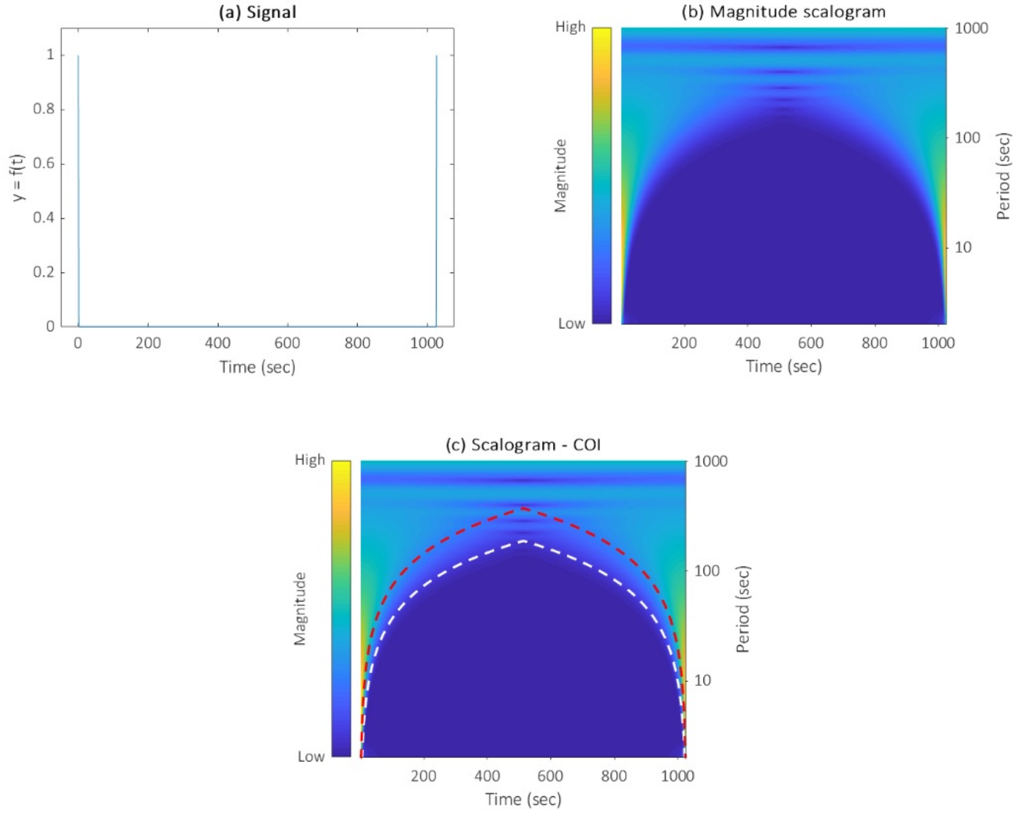

Figure 9: (a) Representation of a synthetic signal composed of a Dirac impulse at each end, (b) cone of influence drawn for these two particular points, and (c) delimitation of the region affected by edge effects, assuming $q_{coi} = e^{-1}$ (red) or $q_{coi} = 0.02$ (white). Adapted from Bitton (2019).

From the wavelet transform variance to the cross-wavelet transform covariance

In the WT, the coefficient at a given scale reflects the contribution of the variance of the signal at a specific time (Kumar & Foufoula-Georgiou, 1994). Averaging the scalogram over time gives the wavelet spectrum, which shows how variance is distributed across scales (Torrence & Compo, 1998) :

$$E_x(j) = \frac{\delta t}{C_\delta} \cdot \frac{1}{N} \sum_{n=0}^{N-1} \left| T^2(a,b) \right| \tag{17}$$

Where $E_x(j)$ is the wavelet spectrum of the signal at scale index j, $T(a,b)$ the wavelet coefficient of the signal at scale a and time b, C_δ an empirically derived, wavelet-specific constant introduced in the reconstruction of a δ-function from its WT (Torrence & Compo, 1998), δt the sampling interval of the time series, and N the number of points in the time series.

From equation (17), integration over all scales gives the total variance of the signal :

$$\sigma_x^2 = \frac{\delta t}{C_\delta} \cdot \frac{\delta j}{N} \sum_{n=0}^{N-1} \sum_{j=0}^{J} \frac{|T^2(a,b)|}{a(j)} \tag{18}$$

Where σ_x^2 is the total variance of the signal in the time domain, δj the scale resolution, and $a(j)$ the jth scale (this term appears in the L^2 norm but is omitted in the L^1 norm).

From the wavelet variance of a single signal, this property can be extended to pairs of signals. In this case, the WT leads to the cross-wavelet transform (XWT), where the same computation applied to two different time series results in their covariance rather than the variance of a single signal. This follows the same principle used in EC flux estimation to relate the simultaneous fluctuations of two quantities. In this context, Schaller et al. (2017) adapted the wavelet spectrum formulation of Torrence and Compo (1998) to define the cross-wavelet spectrum :

$$E_{xy}(j) = \frac{\delta t}{C_\delta} \cdot \frac{1}{N} \sum_{n=0}^{N-1} \left[T_x(a,b) \cdot T_y^*(a,b) \right] \tag{19}$$

Where $E_{xy}(j)$ is the cross-wavelet spectrum between the two signals at scale a_j, $T_x(a,b)$ and $T_y(a,b)$ are the wavelet coefficients of signals x and y at scale a and time b, and $T_y^*(a,b)$ is the complex conjugate of $T_y(a,b)$.

Analogous to Equation (18), integrating the real part of the cross-wavelet spectrum over all scales provides the covariance between the two signals (Stull, 1988; Schaller et al., 2017) :

$$\overline{x'y'} = \frac{\delta t}{C_\delta} \cdot \frac{\delta j}{N} \sum_{n=0}^{N-1} \sum_{j=0}^{J} \frac{\Re \left[T_x(a,b) \cdot T_y^*(a,b) \right]}{a(j)} \tag{20}$$

The covariance is calculated using only the real part of the cross-spectrum, as it reflects the in-phase co-variation between the signals, whereas the imaginary part represents the 90° phase-shifted component (Stull, 1988; Torrence & Compo, 1998). Once again, the term $a(j)$ is omitted in the L^1 normalization. A practical outcome of Equation (20) is that any subset of scales, from $j = 0, 1, 2, \ldots, J$, can be independently selected to quantify the contribution of a specific range of periods to the total covariance (Schaller et al., 2017).

Parameterization of the WT

In this study, the WT was parameterized using the L^1 norm. The main advantage of this normalization is that it preserves the amplitude between the frequency components of the signal and the corresponding wavelet coefficients, which makes it particularly convenient for graphical representation (Bitton, 2019). With L^1 normalization, no scale-dependent correction of the coefficient amplitude is required, allowing a straightforward estimation of fluxes across different scales. In this case $\lambda_{\text{norm}} = \frac{1}{a}$.

The minimal period is chosen as 0.05 which is the period of measurement of the sensors. It is usually advised to set this limit to the Nyquist frequency (Thomas & Foken, 2005). But in the case of this study, the selection of the value was done according to prior tests of the parameter made by Tzvetkov (2023) to minimize the error between the estimation of covariance derived from the WT and EC under stationary conditions. The scale resolution, and the minimum period analyzed were all set to the time step, which is 0.05. The maximum period analyzed was set to one-third of the total signal length, as higher scales would be too affected by edge effects. Finally, the q_{coi} is set at 0.02 as proposed by Nobach et al., (2007).

Conversion from wavelet covariance to flux

To express the covariances obtained from both the WT and EC in standard flux units, a unit conversion is applied. H and LE are expressed in W m^{-2} using air density (ρ_{air}), the specific heat capacity of dry air (c_p), and the latent heat of vaporization of water (L_v). FC is expressed in μmol m^{-2} s^{-1}s using the molar density of air (ρ_{mol}). Fluxes from EC were directly available in standard units from the dataset. Table 1 shows the covariance units from the XWT and the formulas used for the conversion.

Table 1: Conversion from wavelet-derived covariances to fluxes for each scalar.

Scalar	**Unit of wavelet covariance** $(\overline{w'x'})$	**Conversion formula**	**Final unit**
H	$\mathrm{m\,s^{-1}\,K}$	$H = \rho_{\text{air}}\, c_p\, \overline{w'T'}$	$\mathrm{W\,m^{-2}}$
LE	$\mathrm{m\,s^{-1}\,mmol\,mol^{-1}}$	$LE = \rho_{\text{air}}\, L_v\, \frac{M_{\text{H}_2\text{O}}}{M_{\text{air}}}\, 10^{-3}\, \overline{w'\chi'}$	$\mathrm{W\,m^{-2}}$
FC	$\mathrm{m\,s^{-1}\,\mu mol\,mol^{-1}}$	$FC = \rho_{\text{mol}}\, \overline{w'c'}$	$\mathrm{\mu mol\,m^{-2}\,s^{-1}}$

Data process and selection

This analysis used data from the Lonzée and Vielsalm ICOS sites covering the period from January 1, 2020 to December 31, 2020. Although the wavelet transform was applied to the full 24-hour signal, only the coefficients corresponding to the period between 08:00 and 16:00 were retained, in order to focus on daytime convective conditions. For the comparison of flux patterns throughout the year, a narrower interval between 10:00 and 14:00 was used. The choice of this time range is intended to exclude transitional effects in the morning and evening and to provide a consistent basis for inter-day comparison throughout the year, including winter.

The investigated period range extends from 0.05 seconds to 3 (2 h 57 min 26 s) hours. The lower limit is defined by the instrumental resolution at high frequencies, while the upper limit corresponds to the highest scale outside the cone of influence for all hours during the daytime window (08:00 to 16:00), which was the initial focus of the study, with q_{coi} = 0.02. For direct comparison between the WT and EC, the fluxes are also estimated over averaging periods ranging from 0.05 to 30 minutes (29 min 16 s) using the WT.

Spike detection and replacement were performed using thresholds of $\omega = 5$ for horizontal wind components and $\omega = 3.5$ for temperature, χ and CO_2. Each half-hour segment was processed independently, and periods with more than 1% of flagged spikes were excluded following Foken (2008). Days containing such segments were consequently discarded.

During data processing, it was found that some half-hour periods were filled with zeros. Days containing such replacements near the periods of interest were excluded from the analysis, as they were found to occasionally generate artifacts in the WT coefficients in the surrounding segments. The only available quality flag on the server was the steady-state and test and integral turbulence characteristics (SSITC) test which proved effective in filtering out the majority of unreliable results. The details of this specific test are provided in Appendix 2. As H and LE were necessary to calculate the EBR, only half hours passing the test for both were kept. This resulted in 116 and 134 valid days for Lonzée and Vielsalm, respectively.

To assess the influence of meteorological drivers on the magnitude of mesoscale contribution, the ranges of temperature, wind speed, stability (z/L), and friction velocity (u^*) observed at Vielsalm were divided into 15 linearly spaced groups (or bins). For each group, EBR values were calculated using both the WT method and the classical EC method, applying the same binning procedure. This approach enabled a direct comparison of their responses under similar conditions.

Computing

Applying the XWT to day-long high-frequency measurement series requires significant computing power. To broaden the scope of the analysis, the CECI was used to perform these computations. The CECI is a consortium of supercomputers that brings together the computing power of five universities in the Walloon Region of Belgium.

The cluster's architecture allows both parallel execution of several processing runs, referred to as jobs, across different nodes, and multi-threaded execution within each job. This is particularly convenient, as the library used for the WT, pyFFTW, natively supports multi-threading. This dual-level parallelisation, combined with the large available memory makes it possible to run the WT on large, year-long datasets within a reasonable time frame. More details on the workflow used to run the computations on the CECI are provided in Appendix 3.

3 Results

3.1 Assessment of the energy imbalance at the study sites

Ordinary least squares (OLS) regression analysis based on the highest quality criteria according to the SSITC test on half-hours between 10:00 and 14:00 showed a systematic underestimation of the turbulent fluxes ($H + LE$) relative to available energy ($R_{\text{net}} - G - S$) at both study sites (see Figure 10).

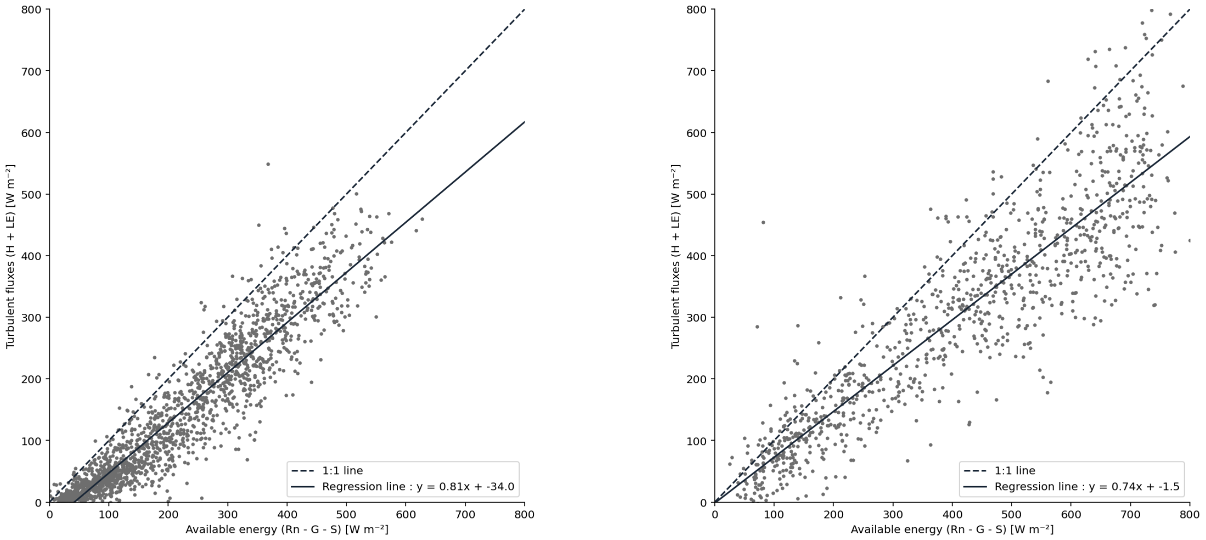

(a) Lonzée (b) Vielsalm

Figure 10: Energy balance closure at the two study sites. OLS regression between turbulent fluxes ($H + LE$) and available energy ($R_{net} - G - S$) for half-hourly data between 10:00 and 14:00. The dashed line represents the 1:1 line, while the continuous line indicates the OLS regression.

At Lonzée, the slope of the linear regression between turbulent fluxes and available energy is 0.81, with a negative intercept of -34 W m^{-2}. The yearly EBR value is 0.65. In addition, 96.76 % of the half-hours fall below the bisector of the first quadrant, indicating a systematic energy deficit. The mean energy imbalance between available energy and turbulent fluxes is – 34.76 W m^{-2} for Lonzée. The mean net radiation for 2020 recorded at this site is 267.7 W m^{-2}, with a maximum half-hourly value of 702.4 W m^{-2}.

At Vielsalm, the regression slope is slightly lower at 0.74, with a near-zero intercept of -1.5 W m^{-2}. The EBR reaches 0.73, indicating better, though still incomplete, closure. Nevertheless, 90.04 % of the half-hours contained in the analysis fall below the bisector of the first quadrant, and the average energy imbalance at this site is -26.04 W m^{-2}. The mean net radiation recorded at Vielsalm is higher than at Lonzée amounting to 416.2 W m^{-2}, with a maximum of 881.6 W m^{-2}.

3.2 Comparison of flux estimates from EC and the WT methods

Table 2 and 3 shows the comparison between fluxes estimated using the EC method, based on a 30-minute averaging period, with those reconstructed from the WT, which includes periods ranging from 0.05 seconds up to approximately 30 min for $\mathrm{WT}_{30\ \mathrm{min}}$ and up to 3 hours for $\mathrm{WT}_{3\ \mathrm{h}}$ for Lonzée and Vielsalm, respectively.

Table 2: Comparison of fluxes estimated with EC and WT methods for Lonzée

Flux	Method	Mean	EC – WT	Mesoscale proportion
H	EC	109.90 W m^{-2}	—	—
	$\mathrm{WT}_{30\ \mathrm{min}}$	113.73 W m^{-2}	-3.82 W m^{-2}	—
	$\mathrm{WT}_{3\ \mathrm{h}}$	115.62 W m^{-2}	-5.72 W m^{-2}	1.70 %
LE	EC	124.40 W m^{-2}	—	—
	$\mathrm{WT}_{30\ \mathrm{min}}$	76.67 W m^{-2}	$+47.73$ W m^{-2}	—
	$\mathrm{WT}_{3\ \mathrm{h}}$	77.49 W m^{-2}	$+46.91$ W m^{-2}	1.12 %
FC	EC	-6.66 μmol m^{-2} s^{-1}	—	—
	$\mathrm{WT}_{30\ \mathrm{min}}$	-5.11 μmol m^{-2} s^{-1}	-1.54 μmol m^{-2} s^{-1}	—
	$\mathrm{WT}_{3\ \mathrm{h}}$	-5.06 μmol m^{-2} s^{-1}	-1.59 μmol m^{-2} s^{-1}	-0.95 %

Table 3: Comparison of fluxes estimated with EC and WT methods for Vielsalm.

Flux	Method	Mean	EC – WT	Mesoscale proportion
H	EC	246.32 W m^{-2}	—	—
	$\mathrm{WT}_{30\ \mathrm{min}}$	243.70 W m^{-2}	$+2.62$ W m^{-2}	—
	$\mathrm{WT}_{3\ \mathrm{h}}$	254.77 W m^{-2}	-8.45 W m^{-2}	4.71 %
LE	EC	127.58 W m^{-2}	—	—
	$\mathrm{WT}_{30\ \mathrm{min}}$	116.64 W m^{-2}	$+10.95$ W m^{-2}	—
	$\mathrm{WT}_{3\ \mathrm{h}}$	122.35 W m^{-2}	$+5.23$ W m^{-2}	5.11 %
FC	EC	-11.43 μmol m^{-2} s^{-1}	—	—
	$\mathrm{WT}_{30\ \mathrm{min}}$	-9.90 μmol m^{-2} s^{-1}	-1.53 μmol m^{-2} s^{-1}	—
	$\mathrm{WT}_{3\ \mathrm{h}}$	-10.37 μmol m^{-2} s^{-1}	-1.06 μmol m^{-2} s^{-1}	5.00 %

Sensible heat

For H, the fluxes estimated using the WT are similar to those derived from EC at both Lonzée and Vielsalm.

At Lonzée, the $\mathrm{WT}_{30\ \mathrm{min}}$ showed a slight overestimation of 3.82 W m^{-2} for the sensible heat on average compared to EC. When the mesoscale contribution was included, this difference increased to 5.72 W m^{-2}. The magnitude of the mesoscale H was only 1.70 % of that of the microscale flux.

For Vielsalm, the $\mathrm{WT}_{30\ \mathrm{min}}$ underestimated sensible heat flux by 2.62 W m^{-2} on average. The inclusion of mesoscale contribution, as for Lonzée, led to a positive increase of the flux estimate. This resulted in $\mathrm{WT}_{3\ \mathrm{h}}$ giving a higher estimation of the fluxes of 8.45 W m^{-2}. The proportion of mesoscale H compared to the microscale flux was more than twice higher than for Lonzée, with a result of 4.71 %.

Latent heat

At Lonzée, the estimation of LE from both $\mathrm{WT}_{30\ \mathrm{min}}$ and $\mathrm{WT}_{3\ \mathrm{h}}$ shows a substantial underestimation compared to the EC method, with average differences of about 47 $\mathrm{W\,m^{-2}}$. Despite this marked gap, the relative contribution of mesoscale motions remains limited, accounting for only 1.12 % of the microscale flux, lower than the proportion observed for sensible heat at the same site.

At Vielsalm, the differences between WT and EC estimates are smaller. The $\mathrm{WT}_{30\ \mathrm{min}}$ underestimates LE by 10.95 $\mathrm{W\,m^{-2}}$ on average, while the inclusion of mesoscale contribution reduces this gap to 5.23 $\mathrm{W\,m^{-2}}$. The mesoscale component represents 5.11 % of the microscale flux in this case, a value comparable to that found for sensible heat at this site.

CO_2 fluxes

The same trend as for energy fluxes is observed for FC. Both sites showed an underestimation in terms of magnitude for the estimation of the CO_2 fluxes with the WT compared to EC.

At Lonzée, the $\mathrm{WT}_{30\ \mathrm{min}}$ and $\mathrm{WT}_{3\ \mathrm{h}}$ produced nearly identical estimates, suggesting a negligible contribution from mesoscale motions.

At Vielsalm, the wavelet estimates were also lower than EC, but a negative contribution from mesoscale motions was observed. This additional component represented about 5 % of the microscale flux, consistent with the proportions found for H and LE at the same site.

Unexpected results at Lonzée

The considerable underestimation of LE prevented a meaningful comparison of EBR as the WT systematically showed very low EBR values. Considering this issue, along with the low mesoscale contribution in Lonzée (Table 2), the following analysis will only focus on the site of Vielsalm.

3.3 Comparison of the energy balance closure from the two methods

Figure 11 presents the monthly evolution of the EBR derived from EC, and from the WT estimates both with ($\mathrm{WT}_{3\ \mathrm{h}}$) and without ($\mathrm{WT}_{30\ \mathrm{min}}$) mesoscale contribution.

Monthly EBR estimated from EC shows a progressive increase from 0.62 in March to a maximum of 0.81 in August, before slightly decreasing in September. The highest monthly EBR for EC follows in November with a value of 0.85.

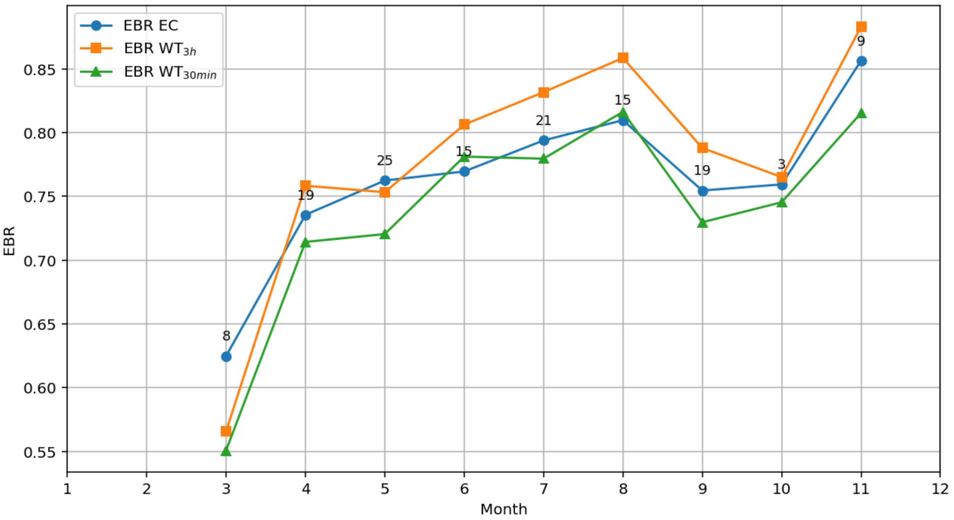

Figure 11: Mean monthly EBR derived from EC, WT$_{30\ \mathrm{min}}$, and WT$_{3\ \mathrm{h}}$. The indices above the markers indicate the number of days included in the monthly average.

Monthly EBR estimates from WT$_{30\ \mathrm{min}}$ were on average 3.3 % lower than those from EC throughout the study period. Exceptions occurred in June and August, when WT$_{30\ \mathrm{min}}$ produced slightly higher values of 1.5 % and 0.8 %, respectively.

Except for the months of March and May, the monthly EBR derived from WT$_{3\ \mathrm{h}}$ is systematically higher than that from EC. In addition, WT$_{3\ \mathrm{h}}$ consistently produces higher monthly EBR values than WT$_{30\ \mathrm{min}}$.

The largest discrepancy is observed in March, where the EBR from WT$_{30\ \mathrm{min}}$ is 11 % lower than that from EC.

3.4 Quantification of mesoscale contribution

A more detailed analysis showed that mesoscale contribution at Vielsalm were not consistently positive and exhibited some variability in magnitude (see Figure 12).

The median mesoscale contribution is 9.17 $\mathrm{W\,m^{-2}}$ for H and 4 $\mathrm{W\,m^{-2}}$ for LE, while FC exhibits a negative median value of –0.49 $\mu\mathrm{mol\,m^{-2}\,s^{-1}}$. The median mesoscale contributions, positive for H and LE and negative for FC, are aligned with the expected direction of the turbulent fluxes at these times, suggesting a reinforcing rather than a compensatory effect for most half-hours. The interquartile ranges for H and LE are broad, spanning from 4.21 to 16.43 $\mathrm{W\,m^{-2}}$ and –1.18 to 10.81 $\mathrm{W\,m^{-2}}$, respectively, indicating that mesoscale motions can have variable, and in some cases even opposite, effects on energy flux estimates. The mesoscale contribution to FC also showed extreme values of opposite sign contribution to the microscale flux, going up to 3.4 $\mu\mathrm{mol\,m^{-2}\,s^{-1}}$. Figure 13 presents cases of cross-scalograms with mesoscale contributions of opposite sign to the microscales for each scalar.

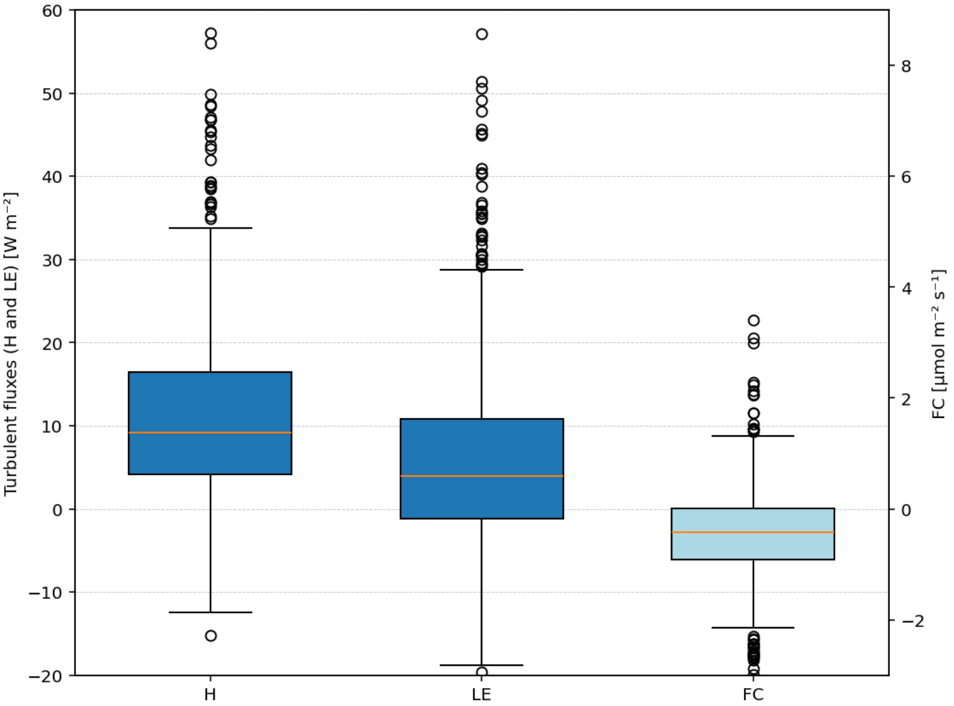

Figure 12: Box plots of mesoscale fluxes of H, LE, and FC at Vielsalm.

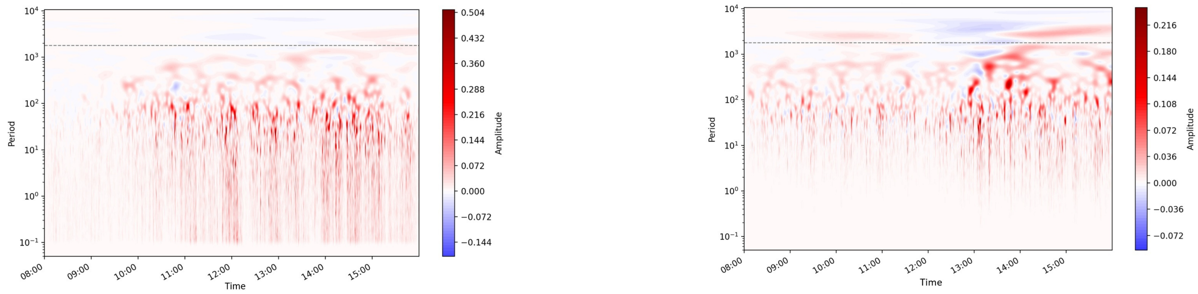

(a) Wavelet cross-scalogram of $w'T'$ on 23 February 2020.

(b) Wavelet cross-scalogram of $w'\chi'$ on 14 August 2020.

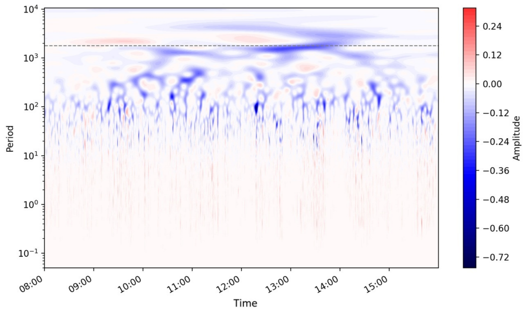

(c) Wavelet cross-scalogram of $w'c'$ on 13 July 2020.

Figure 13: Wavelet cross-scalograms exhibiting mesoscale contributions of opposite sign to the microscales.

3.5 Meteorological conditions leading to the development of mesoscale circulations

The results showed that mesoscale contributions varied according to meteorological conditions. Figure 14 shows the mean mesoscale contribution under different meteorological conditions for H, LE, and FC separately.

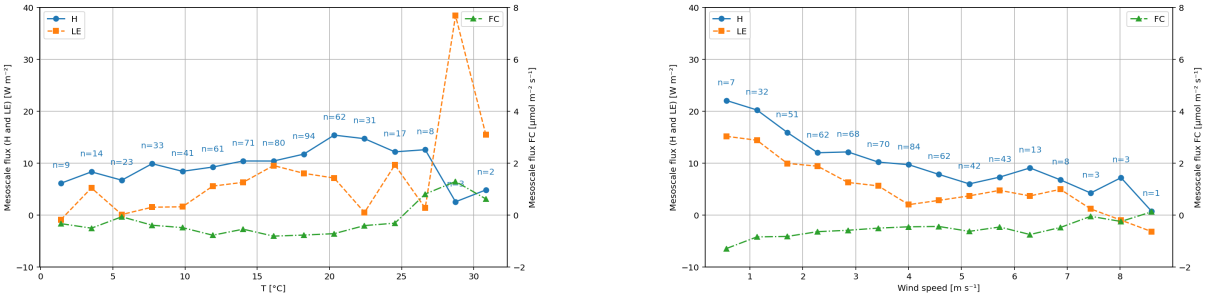

(a) Temperature

(b) Wind speed

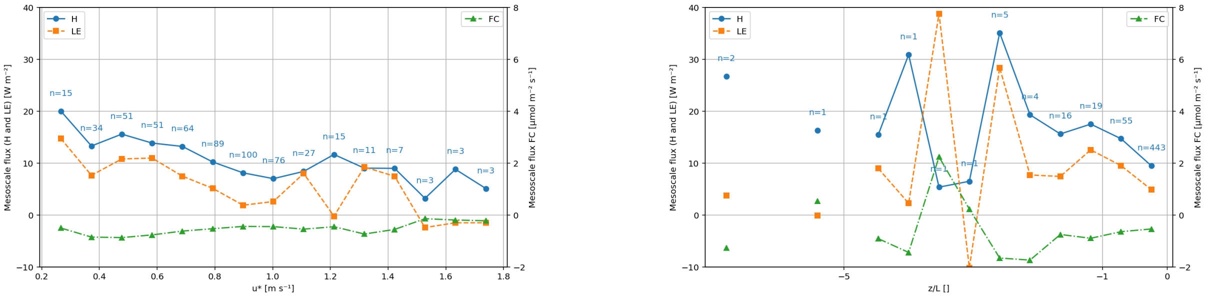

(c) $u*$

(d) z/L

Figure 14: Dependence of mesoscale flux contributions (H, LE, and FC) at Vielsalm on different meteorological conditions. The indices above the markers indicate the number of half-hourly observations included in each bin.

Temperature

For air temperature, the magnitude of mesoscale contributions increases with rising temperature for both H and LE. For H, mesoscale fluxes exceed 10 W m^{-2} between 13 °C and 27 °C, before dropping below this threshold at higher temperatures. For LE, the group centered at 28.7 °C exhibits a peak mesoscale contribution of 38.4 W m^{-2}, averaged over three days (August 1, 9, and 10). This maximum is associated with a reduced contribution from mesoscale H. The mesoscale contribution of FC decreases slightly with rising temperature, reaching its lowest value of –0.81 µmol m^{-2} s^{-1} around the bin centered at 16.1 °C. Beyond this point, the trend reverses, with contributions gradually increasing toward positive values, peaking at 1.3 µmol m^{-2} s^{-1} in the same group centered at 28.7 °C in which the LE peak occurred.

Wind speed

The highest mesoscale contribution to H occurs under low wind speed conditions. The group centered around 0.5 m s^{-1} exhibits a peak value of 22 W m^{-2}, while all groups below 4 m s^{-1} show contributions exceeding 10 W m^{-2}. The magnitude of mesoscale H fluxes consistently decreases with increasing wind speed.

A similar trend is observed for LE : groups below 1.5 m s^{-1} yield mesoscale contributions above 10 W m^{-2}, with values gradually declining as wind speed increases. For both H and LE, mesoscale contributions converge toward zero as wind speed approaches 8.6 m s^{-1}.

The mesoscale contribution to FC follows a similar trend as energy fluxes, with the highest negative value of –1.3 µmol m^{-2} s^{-1} observed in the lowest wind speed bin.

Friction velocity

Mesoscale contributions to H tend to decline with increasing u^*. The highest value, 20 W m^{-2}, is observed in the group with the lowest u^* (0.26 m s^{-1}), while groups with u^* below 0.9 m s^{-1} maintain average contributions above 10 W m^{-2}.

The mesoscale contribution to LE follows a similar decreasing trend with increasing u^*, as observed for H. A slight increase is observed between $u^* = 1.0$ and $u^* = 1.4$ m s^{-1}, with a localized decrease in the group centered at 1.2 m s^{-1}, which mostly includes half-hours from March. Beyond $u^* > 1.5$ m s^{-1}, mesoscale contribution to LE drop to values close to zero.

While relatively stable overall, the mesoscale contribution to FC decreases in magnitude with increasing u^*, and drops to near-zero in the two highest groups ($u^* > 1.5$ m s^{-1}), similarly to LE.

Stability parameter

Most half-hourly periods fell within the last groups, with a total of 443 half-hours corresponding to an unstable regime. No data points were classified as stable, as the analysis was restricted to the time window between 10:00 and 14:00, during which atmospheric conditions are typically convective.

The last group, which contained the largest number of half-hour periods, showed a mesoscale contribution of 9.5 W m^{-2} for H. The magnitude of mesoscale H fluxes generally increases as atmospheric conditions become more unstable ($z/L < -1$), but this trend becomes less consistent in the most unstable groups, which include fewer data points. The group showing the highest flux (35.1 W m^{-2}), centered at $z/L = -2.6$, contains 8 half-hours.

For LE, the same trend as for H was observed, although a shift occurred for the group centered at $z/L = -3$, with a highly negative contribution of –10.1 W m^{-2} on 12 May, followed by the highest positive contribution of 38.8 W m^{-2} on 8 August. These two dates were associated with H contributions lower than 10 W m^{-2}.

For FC, the mesoscale contribution increases in magnitude as atmospheric conditions become more unstable, reaching its lowest value around $z/L = -2.6$. Beyond this point, the following groups exhibit shifts in the sign of the contribution.

3.6 Contribution of mesoscale motions to energy balance closure

Figure 15 illustrates the differences in EBR estimations between the $WT_{3\text{ h}}$ and EC methods across the same meteorological bin groups as Figure 14.

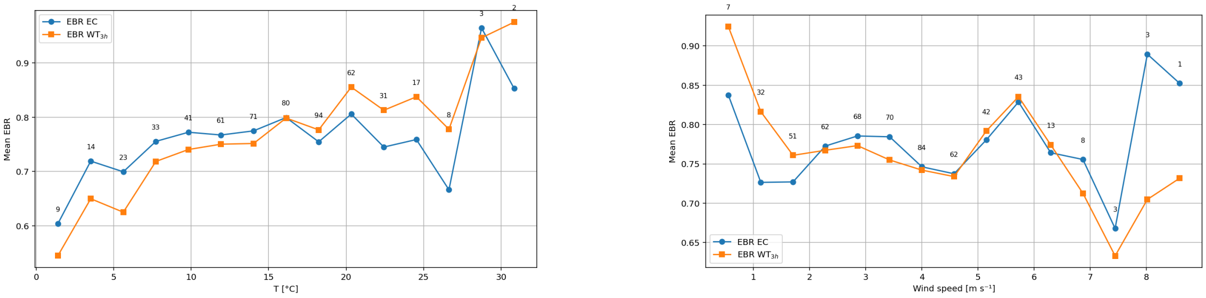

(a) Temperature (b) Wind speed

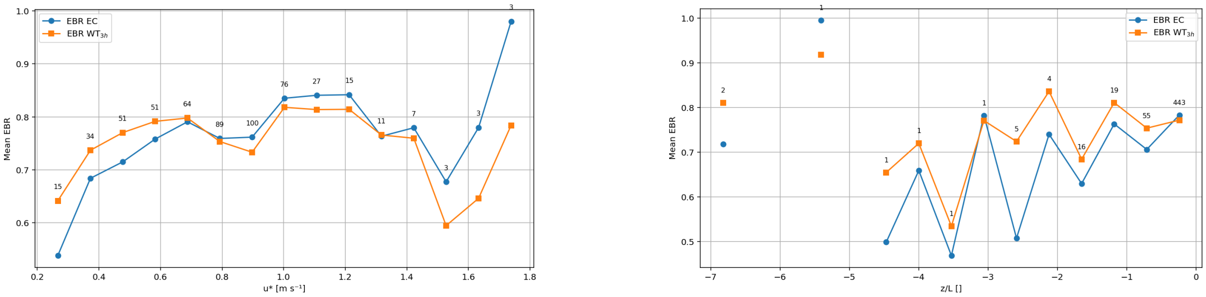

(c) u^* (d) z/L

Figure 15: Variation of the EBR at Vielsalm under different meteorological conditions, comparing EC and $WT_{3\text{ h}}$ estimates. The indices above the markers indicate the number of half-hourly observations included in each bin.

Temperature

The EBR derived from EC is higher than that from $WT_{3\text{ h}}$ for the lower temperature groups up to 16.1 °C, with an average difference of +0.04. From 16.1 °C onward, $WT_{3\text{ h}}$ consistently yields higher EBR values than EC, with an average difference of the same value (+0.04). An exception occurred for the bin centered at 28.7 °C, where the EC-derived EBR slightly exceeds $WT_{3\text{ h}}$ by +0.018.

Wind speed

The EBR derived from $\mathrm{WT}_{3\,\mathrm{h}}$ is higher than that from EC for wind speed groups below 2 m s^{-1}, with these three groups showing an average increase of +0.07. For higher wind speed groups, the EBR values are generally similar between both methods. However, a notable difference is observed in the last two bins. All four half-hour periods in these groups correspond to May 11th, a day for which no significant mesoscale contribution was detected. The observed underestimation from $\mathrm{WT}_{3\,\mathrm{h}}$ compared to EC during those periods thus originates solely from the microscale component.

Friction velocity

For u^{*}, a higher EBR is obtained with $\mathrm{WT}_{3\,\mathrm{h}}$ when the value is below $0.7\,\mathrm{m\,s^{-1}}$, with an average EBR increase of 0.05. Above this threshold, the EBR from both methods is similar, with $\mathrm{WT}_{3\,\mathrm{h}}$ yielding slightly lower values. The last three groups, with a mean u^{*} above $1.4\,\mathrm{m\,s^{-1}}$, show a marked difference, with $\mathrm{WT}_{3\,\mathrm{h}}$ producing EBR values lower by 0.14 compared to EC. The dates included in these groups are from May 11th and two half-hours in March.

Stability parameter

The largest group by far is the last one, centered around -0.24 and accounting for 443 half-hours. In this group, the EBR derived from EC is only slightly higher on average. However, as z/L decreases to lower values and a more turbulent regime, $\mathrm{WT}_{3\,\mathrm{h}}$ shows higher EBR values. For $z/L < -1$, the EBR is 0.07 higher for $\mathrm{WT}_{3\,\mathrm{h}}$.

4 Discussion

4.1 Preliminary insights from the results

The comparison between EC and WT indicates a general tendency for the WT, as applied in this study, to underestimate all scalar fluxes. This effect is particularly pronounced for LE at Lonzée. The large discrepancy in LE, along with the significantly lower EBR obtained from WT estimates, led to the abandonment of further analysis for this site. The correlation between LE flux estimates from both methods suggests that the difference seems to be due to a multiplicative factor. This was unexpected, given that Vielsalm did not exhibit the same issue despite the identical processing applied to both sites.

Regardless of the systematic underestimation of fluxes, the proportion of mesoscale contribution appears consistent, and visual inspection of the cross-scalograms confirmed the infrequent occurrence of significant mesoscale contribution at Lonzée. At Vielsalm, $\mathrm{WT}_{30\ \mathrm{min}}$ also systematically underestimated fluxes compared to EC, especially for FC where the difference was higher than 10 %. For instance, Schaller et al. (2017) found deviations of less than 2 % between EC and wavelet, with a maximum scale of 34 minutes, under well-developed turbulence and steady-state conditions. However, despite the higher deviations observed, they remain within the typical uncertainty range of EC fluxes, generally estimated at 5–10 % due to differences in flux processing or gap filling approaches (Foken et al., (2006); Ueyama et al., 2012). The higher EBR observed with $\mathrm{WT}_{3\ \mathrm{h}}$ results from the positive mesoscale contributions to H and LE. This suggests that, if the issue indeed stems from an overall underestimation by the WT, the EBR could be even higher when lower-frequency contributions are accounted for.

Another unexpectedly low value concerns the shortwave incoming radiation at Lonzée, which is substantially lower than at Vielsalm, despite the two sites being only $\sim$90 km apart. This difference directly influences the available energy estimates and would further bias the EBR at Lonzée. An erroneous estimation of radiation is unlikely, as this measurement is generally considered the most accurate, especially around midday (Twine et al., 2000; Foken, 2008). Even when accounting for this possible underestimation of the available energy, a negative intercept is observed at Lonzée. This implies that either S or G is being strongly underestimated. However, these two terms typically account for a small fraction of the available energy (Twine et al., 2000; Jarvis et al., 1997). The storage in the biomass was not included, but for a low-vegetation site, Oncley et al. (2007) found this term to be negligible. These results prompted further analysis to be conducted only for Vielsalm.

4.2 Comparison with other studies

The energy balance at both sites remains unclosed even as the analysis only revolved around daytime hours. This is consistent with the findings of Franssen et al. (2010) and Wilson et al.

(2002) and is one of the main reasons why studying those periods is relevant for the understanding of the energy balance non-closure (Stoy et al., 2013).

The yearly EBR amounted to 0.73 at Vielsalm, and to a lower score of 0.65 at Lonzée. These EBR values are relatively low compared to results from other studies conducted across multiple sites (Barr et al., 2006; Falge et al., 2001; Franssen et al., 2010; Wilson et al., 2002; Stoy et al., 2013). However, Stoy et al. (2013) also found that the lowest EBR values were typically observed over mixed forest and cropland ecosystems (compared to savannas and broadleaf forests). The specific topography of Vielsalm is also to be taken into account, and previous campaigns carried out over a valley (Eigenmann et al., 2011; Brötz et al., 2014) found a residual energy of 21 %.

One key observation is that mesoscale fluxes were almost systematically detected on the tower of Vielsalm but not at Lonzée. This difference can partly be attributed to the measurement height. According to standard practice, the sonic anemometer should be positioned at approximately twice the canopy height. This led to the sonic anemometers standing at 2 m high for Lonzée and 51 m high for Vielsalm. As previously discussed, the measurement height at Vielsalm, while being lower than this standard guideline, is sufficient to ensure that the footprint of the fluxes falls within the intended forested area. This difference in altitude has a consequent impact on the range of eddies to be encountered (Kaimal & Finnigan, 1994; Lee et al., 2005; Foken, 2006a). This is mainly explained by the frictional breaking of the bigger eddies by the surface which prevents them from fully developing near the ground (Högström, 1988). Consequently, larger eddies are more prevalent at higher altitudes. This vertical shift in altitude leads to a shift in the spectral gap. At higher measurement heights, turbulent energy is shifted towards lower frequencies, consistent with findings by Anderson et al. (1984) and Baldocchi and Meyers (1988). This height-dependence has been recognized as a significant factor in influencing the EBC (Liu et al., 2024; Lee and Black, 1993). This can be explained by the larger, stronger flow produced by larger vertical winds found at higher elevations (Kanda et al., 2004). Therefore, the frequency range where the spectral gap is expected to occur should be reconsidered in relation to the instrumentation height used at each site.

Another factor explaining the energy balance non-closure at Vielsalm is its specific canopy layer. Intermittent coherent structures have been observed above tall forest canopies (Gao et al., 1989; Högström et al., 1989; Raupach et al., 1989) and are known to play a role in the transport of momentum and scalars both above and within forest canopies (Gao et al., 1989; Finnigan et al., 2003). These structures typically consist of two phases: a slow upward movement, referred to as an ejection, followed by a fast downward motion known as a sweep (Thomas & Foken, 2005). Such events could exacerbate the energy balance non-closure, as they may lead to undetected circulations. For instance, the sudden outburst associated with sweeps might be flagged as spikes and removed during data processing, while the slower ejections might go undetected by EC. Gao et al. (1989) also demonstrated that the intensity of sweeps and ejections varies with height.

While sweeps dominate near the canopy top, their contribution tends to balance with that of ejections around twice the canopy height (Gao et al., 1989). This further explains the standard measurement height. Nevertheless, despite these limitations, the overall impact of coherent structures on flux estimates remains relatively small. According to Thomas and Foken (2007), the flux error associated with such coherent structures is less than 4 % for the EC method.

The quantification of mesoscale transport revealed a higher contribution to H than to LE in terms of magnitude. This finding corroborates the results of Charuchittipan et al. (2014) and Mauder (2020), who reported that mesoscale corrections generally have a stronger impact on H than on LE. However, in terms of proportion, the contributions appear similar. As shown in Figure 12, mesoscale contributions span both positive and negative values for H, LE, and FC. At the half-hourly scale, these contributions can either improve or deteriorate the surface EBC. This dual effect is consistent with the observations of Gao et al. (2016), who noted that the inclusion of larger eddies may either enhance or reduce the EBC.

4.3 Topographic influences on mesoscale contributions

The greater occurrence of mesoscale fluxes at Vielsalm can also be explained by the topography of the site. Lonzée is characterized by relatively homogeneous and flat terrain, whereas the Vielsalm tower is located on the flank of a valley. This specific topographic setting results in a unique microclimate and airflow regime driven by the interaction between surface geometry and the diurnal–nocturnal cycle. Valley slopes can generate thermally driven circulations. At night, katabatic flows (from Greek *katá*, “downward”, and *baínō*, “to go”) develop as the slope surface cools radiatively, causing dense, cold air to slide downslope. Conversely, during the day, solar heating of the slope induces anabatic flows (*aná*, “upward”), where warmer, lighter air rises upslope (Stull, 1988). These thermally induced advections escape detection by EC, and it is worth noting that shifts in wind direction due to such flow transitions could lead to non-stationarity (Turnipseed et al., 2004). Since the wavelet transforms covered periods up to 3 hours, part of this advective transport may therefore have appeared as low-frequency contributions to H and LE. In a previous study, Turnipseed et al. (2002) observed better EBC during anabatic flow compared to katabatic flow. While the occurrence of an anabatic flow could potentially generate advection-driven upward positive fluxes that remain undetected by the EC method, such flows typically develop under daytime convective conditions. This result might therefore be a consequence of the meteorological conditions under which it occurs rather than of the flow itself. Thomas and Foken (2005) also related some of the transport of scalars by lower frequencies to horizontal transport, as they found better similarity between spectra of scalars and horizontal velocity than with those of vertical velocity in the low frequencies over a spruce forest.

Another notable microclimatic phenomenon associated with valleys may also be at play, especially during autumn and winter. After sunset, and throughout the night, katabatic flow tends to accumulate colder air at the bottom of the valley, forming a thermal inversion where cooler air is trapped below warmer layers. After sunrise, if buoyancy forces are insufficient to fully mix the atmosphere, this inversion layer may be lifted up and remain suspended above the valley, effectively capping it, as illustrated in Figure 16. This stable, stratified layer creates a closed system, limiting vertical mixing unless the inversion is broken by strong enough convective forcing (Stull, 1988).

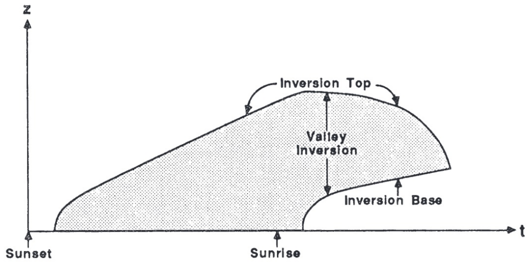

Figure 16: Evolution of valley inversion. Adapted from Stull (1988).

This phenomenon is well documented in urban valleys, as it can lead to excessive pollutant accumulation over urban areas (Rendón et al., 2015). Inversion layers can induce specific circulation patterns, such as gravity waves (Turnipseed et al., 2004), which are typically observed near the tropopause via aircraft measurements (F. Zhang et al., 2015). However, a floating inversion over valleys may induce similar wave-like behavior near the surface. As this specific microclimate requires low turbulence, it is more likely to occur during colder periods of the year or at night.

4.4 Meteorological drivers of mesoscale circulations

Over the site of Vielsalm, mesoscale contributions were more frequently detected under low wind speed, low u^*, as well as higher temperature. This matches the expected conditions where buoyancy-driven turbulence dominates (Li & Bou-Zeid, 2011; Dupont et al., 2024), allowing thermally induced mesoscale circulations to emerge at specific locations depending on surface heterogeneities (Kanda et al., 2004; Sühring & Raasch, 2013; Stull, 1988; Stoy et al., 2013). Evidence of mesoscale formation linked to heterogeneity has been observed in multi-tower experiments (Mauder et al., 2010) and associated with poorer EBC (Panin et al., 1998; Mauder et al., 2007b).

The impact of heterogeneities can be reduced by moderate wind speed, depending on the wind direction relative to the surface pattern (Letzel & Raasch, 2003). In this study, a lower magnitude of mesoscale contribution at Vielsalm coincides with generally higher wind speeds, suggesting a possible dilution of horizontal gradients of heterogeneity, as described by Avissar and Schmidt (1998). Conversely, low-to-moderate winds favor the persistence of mesoscale structures, which could generate low-frequency positive contributions to the vertical heat flux $w'T'$. If the timescale of such mesoscale events exceeds the EC averaging period, their contribution is no longer captured as turbulent fluctuations but instead appears in the mean vertical heat flux $\overline{w}\overline{T}$ (Stoy et al., 2013), violating the stationarity assumption. Fluxes at these time scales would therefore be unaccounted for from the turbulent flux estimates by EC (Panin et al., 1998; Mauder et al., 2007b; Lee, 1998; Sun et al., 1998) and help explain the higher EBR of $\mathrm{WT}_{3\,\mathrm{h}}$ for low wind speed.

As noted by Li & Bou-Zeid (2011), the magnitude of ejections becomes more efficient than sweeps in producing turbulent fluxes as instability increases. This mechanism can explain the peaks in mesoscale H and LE observed under highly negative z/L and, in turn, explain the results found by Stoy et al. (2013), who reported a drop in EBC from 0.8 under near-neutral conditions to 0.7 under highly convective conditions.

u^* was also a relevant factor. Lower u^* values coincided with higher mesoscale contributions. Since low u^* reflects weaker turbulent mixing, this condition may allow mesoscale motions to contribute more significantly and further reduce the validity of the ergodic assumption (Franssen et al., 2010). Moreover, vertical velocity variance tends to increase with height above the surface (Högström et al., 2002), meaning that the low u^* at the Vielsalm tower combined with its higher measurement height could further enhance the magnitude of mesoscale transport. Previous findings show that EBC tends to be better under higher u^* (Goulden et al., 1997; Wilson et al., 2002; Barr et al., 2006) and that FC estimates under low u^* are less reliable (Barr et al., 2006). This could be partly explained by the increased importance of low-frequency transport observed during such conditions, as shown in Figure 14.

The trend of mesoscale FC generally follows that of the energy fluxes, but the largest peaks in LE are often associated with positive mesoscale contributions to FC. This complex correlation can be explained by differences in the underlying processes (Zhou et al., 2024; Li & Bou-Zeid, 2011). FC and LE are typically correlated when both are driven by stomatal fluxes (Scanlon & Sahu, 2008). However, once the plant reaches its physiological limit and stomata close, LE may increasingly originate from soil evaporation, while the positive mesoscale contribution to FC could result from enhanced soil respiration, which is known to increase exponentially with temperature (Lloyd & Taylor, 1994; Reichstein et al., 2003). This interpretation is consistent with the observed decoupling of these scalars (Li & Bou-Zeid, 2011; Katul et al., 1998). This change in the sign of the correlation is most evident when LE becomes increasingly positive and FC shifts from negative to positive mesoscale values under the highest temperature conditions and in highly unstable regimes (Figure 14a,d).

5 Conclusion

This study aimed to investigate the contribution of mesoscale motions to the EBC at two ICOS sites in Belgium, a cropland in Lonzée and a mixed forest in Vielsalm, by applying the WT to high-frequency EC data. The motivation stemmed from the systematic underestimation of turbulent fluxes by EC (Twine et al., 2000; Wilson et al., 2002; Aubinet, 2012; Foken, 2008) and the hypothesis that low-frequency motions beyond the standard 30-minute averaging period are partly responsible for this imbalance (Mauder et al., 2020; Panin et al., 1998; Stoy et al., 2013).

The results confirmed a systematic lack of EBC at both sites, with yearly EBR values of 0.65 at Lonzée and 0.73 at Vielsalm. While WT flux estimates tended to underestimate the magnitude of EC fluxes overall, the decomposition of fluxes by scale revealed that mesoscale contributions were consistently present at Vielsalm but negligible at Lonzée. At Vielsalm, mesoscale fluxes represented on average 5 % of the microscale fluxes for H, LE, and FC, occasionally reaching higher magnitudes under specific meteorological conditions such as high temperatures, low wind speeds, low u^*, and highly unstable regimes. Their inclusion generally improved EBC, with WT3h yielding higher EBR values than EC, particularly when mesoscale contribution reached 10 $\mathrm{W\,m^{-2}}$ and more. The mesoscale contributions to FC were correlated with those of H and LE up to a threshold of atmospheric conditions. Under highly unstable regimes and higher temperatures, the relationship weakened or even reversed, reflecting a decoupling between water vapor and carbon fluxes once stomatal regulation reached its physiological limits and soil processes became dominant (Li & Bou-Zeid, 2011). These findings highlight the complexity of scalar correlations and the importance of site-specific factors in mesoscale dynamics. The absence of significant mesoscale contributions at Lonzée can be attributed to its flat, homogeneous terrain and low measurement height, whereas the complex topography and higher sensor placement at Vielsalm favor the development and detection of larger-scale eddies. This emphasizes the need to reconsider the universality of the spectral gap (Destouet et al., 2024).

Despite these findings, several limitations remain. Although the whole year was considered, most days turned out to be unsuitable for analysis. The use of the SSITC test as a filtering criterion ensured reliability but introduced a selection bias, since some days with low stationarity, potentially linked to stronger mesoscale contributions (Mahrt, 1998; Panin et al., 1998; Mauder & Foken, 2020), were also discarded. As a result, the procedure may have removed precisely the periods most likely to exhibit the strongest mesoscale effects.

The analysis was restricted to 10:00–14:00 to include shorter days while avoiding the morning transition. Yet the wavelet transform is particularly well suited for such non-stationary periods (Daubechies, 1990; Torrence & Compo, 1998). While the possible presence of gravity waves was mentioned for valley sites, even a flat site like Lonzée can experience a residual morning stable layer forming an inversion zone above the canopy. Dupont et al. (2024) showed with Large

Eddy Simulation (LES) that such transitions are shaped by low-altitude entrainment, strongly influencing ecosystem–atmosphere exchanges. Applying the WT to these periods could provide empirical support for these processes and improve the quantification of nighttime ecosystem respiration. Beyond the exclusion of transitional periods, another temporal limitation lies in the maximum scale considered. The maximum period included in this study was three hours to remain under the COI borders, but longer periods could be considered. Mauder and Foken (2006) showed that extending the averaging period up to 24 hours over a maize field almost closed the energy balance. One way to further push back the COI would be to concatenate data series from several consecutive days so that the central day's coefficients remain valid at higher scales. The main limiting factor is memory usage. Tzvetkov (2023) proposed a moving-window approach to overcome this constraint, applying the wavelet transform to shorter segments and recombining the coefficients. Combined with high-performance computing, as in the present study, such methods could make the analysis of timescales up to 24 hours feasible.

In conclusion, mesoscale motions were found to contribute to the EBC at the forest site but not substantially at the cropland site, underlining the relevance of site-specific meteorological conditions. At the same time, their variability with temperature, wind speed, u^*, and z/L further illustrates how meteorological conditions modulate these processes. Ultimately, the results highlight the potential of the wavelet transform to uncover dynamics that remain hidden to the conventional EC method, opening new perspectives for a deeper understanding of ecosystem–atmosphere exchanges.

6 Appendices

6.1 Reynold's decomposition

The Reynolds decomposition separates an instantaneous variable into two components: a mean part and a fluctuating part (Aubinet, 2012).

$$A = \overline{A} + A', \tag{21}$$

where

$$\overline{A} = \frac{1}{T}\int_{t}^{t+T} A(t)\, dt. \tag{22}$$

The application of the Reynolds's decomposition relies on the validity of a set of averaging rules. Those are called the Reynolds's postulates.

Postulate 1

$$\overline{A'} = 0 \tag{23}$$

Over the averaging period, the mean of the fluctuations is, by definition, equal to zero. This follows directly from the definition of those fluctuations, so their positive and negative deviations from the mean cancel each other out.

Postulate 2

$$\overline{AB} = \overline{A}\,\overline{B} + \overline{A'B'} \tag{24}$$

The mean of a product of two variables equals the product of the mean of those two variables plus the mean of the product of their respective fluctuations. This postulate is dependent on the first one, as from Stull (1988) :

$$\begin{aligned}
\overline{AB} &= \overline{(A + A')(B + B')} && (25)\\
&= \overline{AB} + \overline{A'B} + \overline{AB'} + \overline{A'B'} && (26)\\
&= \overline{A}\,\overline{B} + \overline{A'}\,\overline{B} + \overline{A}\,\overline{B'} + \overline{A'B'} && (27)\\
&= \overline{A}\,\overline{B} + 0 + 0 + \overline{A'B'} && (28)\\
&= \overline{A}\,\overline{B} + \overline{A'B'} && (29)
\end{aligned}$$

The terms $\overline{A'}\,\overline{B}$ and $\overline{A}\,\overline{B'}$ are equal to 0 only if the mean of the fluctuations is equal to 0.

Postulate 3

$$\overline{\overline{A}} = \overline{A} \tag{30}$$

Postulate 4

$$\overline{a\,A} = a\,\overline{A} \quad \text{if } a \text{ is constant} \tag{31}$$

Postulate 5

$$\overline{A + B} = \overline{A} + \overline{B} \tag{32}$$

These postulates are valid only when the averaging is performed as an ensemble average (Kaimal and Finnigan, 1994), meaning that the set of measurements used to compute the mean are obtained under identical conditions. Since measurements at a single point can't be repeated, ensemble averaging is instead approximated by averaging over a time period during which the conditions remain unchanged. This equivalence between ensemble averaging and time averaging is known as the ergodic hypothesis (Kaimal and Finnigan, 1994). In other words, the eddy covariance method works properly only if the flow remains stationary during the chosen averaging period (Aubinet, 2012).

6.2 SSITC test

This description of the SSITC test comes from Mauder et al. (2008). The test assigns a quality flag to each half-hourly flux according to the results of two separate procedures: the steady-state test and the integral turbulence characteristics test.

The steady-state test (Foken and Wichura, 1996) evaluates the stationarity of a time series during the averaging period. Specifically, it compares the statistical parameters calculated over the entire averaging period with those obtained from six sub-intervals of 5 minutes each.

The covariance of sub-interval i is calculated as :

$$\overline{w'x'}_i = \frac{1}{N}\sum_{j=1}^{N} \left(w_j - \overline{w}_i\right)\left(x_j - \overline{x}_i\right) \tag{33}$$

Where N is the number of samples in the sub-interval, w is the vertical wind speed, x the scalar of interest (e.g. temperature, CO_2, or water vapor), and the overbar denotes the mean over sub-interval i.

The covariance of sub-interval i is calculated as :

$$\overline{w'x'}_i = \frac{1}{N}\sum_{j=1}^{N}(x_{i,j} - \overline{x}_i)(w_{i,j} - \overline{w}_i) = \frac{1}{N}\left[\sum_{j=1}^{N} x_{i,j}w_{i,j} - \frac{1}{N}\left(\sum_{j=1}^{N} x_{i,j}\right)\left(\sum_{j=1}^{N} w_{i,j}\right)\right] \tag{34}$$

The mean of those six covariances over 5-minute periods is calculated as :

$$\overline{w'x'}_{\text{avg}(5)} = \frac{1}{M}\sum_{i=1}^{M}\overline{w'x'}_i \tag{35}$$

Where $M = 6$ is the number of sub-intervals.

The covariance over the entire 30-minute averaging period is calculated as :

$$\overline{w'x'}_{\text{avg}(30)} = \frac{1}{MN}\sum_{i=1}^{M}\sum_{j=1}^{N}(x_{i,j} - \overline{x})(w_{i,j} - \overline{w}) \tag{36}$$

The time series are considered steady-state if the Relative Non-Stationarity index, defined as :

$$RN_{\text{cov}} = \frac{\overline{w'x'}_{\text{avg}(30)} - \overline{w'x'}_{\text{avg}(5)}}{\overline{w'x'}_{\text{avg}(5)}}, \tag{37}$$

is less than 30%. This criterion is applied separately for each scalar.

The second test is the Integrated Turbulence Characteristics (ITC) test and is a measure of the development of turbulence. This estimation relies on the ratio of the standard deviation of a turbulent parameter and its corresponding turbulent flux, which must follow a predictable law.

For a given scalar x:

$$\frac{\sigma_x}{X^*} = c_1\left(\frac{z}{L}\right)^{c_2} \tag{38}$$

where X^* is its dynamic parameter. For example, for temperature, $X^* = T^* = -\overline{w'\theta'}/u_*$ (Foken and Wichura, 1996).

The values of c_1 and c_2 depend on the value of z/L as well as the specific parameter. For further details on the different values, see Mauder et al. (2008).

The ITC quality flag is then calculated as

$$ITC_\sigma = \left|\frac{\left(\frac{\sigma_x}{X^*}\right)_{\text{model}} - \left(\frac{\sigma_x}{X^*}\right)_{\text{measurement}}}{\left(\frac{\sigma_x}{X^*}\right)_{\text{model}}}\right|. \tag{39}$$

The turbulence is considered to be well developed if $ITC_\sigma \leq 30\%$.

6.3 CECI workflow

The CECI clusters are accessed via a secure shell (SSH) connection and operate on a UNIX-based system. The scripts used in this study are written in Python and uploaded to the cluster together with the required input data. Instead of being executed directly within the user's interactive session, the scripts are submitted as job requests to SLURM (Simple Linux Utility for Resource Management).

Each job is launched using a Bash script (e.g., `run_wavelet.sh`), which begins with SLURM directives specifying the resources required for the task, such as the maximum run time, the number of nodes and CPU cores, and the memory allocation needed.

To submit many jobs at once, the SLURM `--array` option was used. Each job in the array is assigned a unique identifier (`SLURM_ARRAY_TASK_ID`), which is then used to select a specific line from an external text file. This text file, generated beforehand, contained information about the site and date for each run. The corresponding entry is assigned to the variable `DATE_TO_ANALYSE`. A Bash script generating a temporary directory was used to run a Python script designed to access input files corresponding to each date, and to adapt to the way measurement data were stored in the database.

The Bash script shown in Listing 1 launched a total of 366 jobs. To avoid overloading the server, however, the number of simultaneously running jobs was restricted to eight, after consultation with a system administrator, by appending a percentage sign (`%8`) to the `--array` option:

```
#SBATCH --array=1-366%8
```

Finally, the last line of the script launches the Python program `wavelet_transform.py`, passing `TMP_DIR` as an argument. Within the Python script, this argument is accessed via :

```
x = sys.argv[1]
```

By using the CECI, it was possible to process a full year of wavelet transform data for three scalars and to generate their corresponding scalograms within 2–3 days.

Listing 1: Example of bash script used to launch the wavelet transform.

```
#!/bin/bash
#SBATCH --job-name=WaveletArray
#SBATCH --time=01:00:00
#SBATCH --ntasks=1
#SBATCH --cpus-per-task=2
#SBATCH --mem=110GB
#SBATCH --partition=batch
#SBATCH --array=1-366%8

# Load modules
```

```
module --purge
module load releases/2020b
module load SciPy-bundle/2020.11-foss-2020b matplotlib

# Threads CPU
export OMP_NUM_THREADS=2
export MKL_NUM_THREADS=2

# Go to working directory
cd /path/to/file/Run/Code

# Read date line
DATE_A_ANALYSER=$(sed -n "${SLURM_ARRAY_TASK_ID}p" liste_dates.txt)

# Extract infos
SITE=$(echo $DATE_A_ANALYSER | cut -d'/' -f1)
YEAR=$(echo $DATE_A_ANALYSER | cut -d'/' -f2)
DAYCODE=$(echo $DATE_A_ANALYSER | cut -d'/' -f3)
DAYCODE_DASHED=$(echo $DAYCODE | tr '_' '-')

# Input and output directories
SRC_DIR="/path/to/file/data/${SITE}/2020_new"
TMP_DIR="/scratch/SURF/temp_data/${SITE}_${YEAR}_${DAYCODE}"
OUTPUT_DIR="/path/to/file/outputs/${DATE_A_ANALYSER}"
mkdir -p $TMP_DIR
mkdir -p $OUTPUT_DIR

# Copy needed files
find "$SRC_DIR" -type f -name "${YEAR}-${DAYCODE_DASHED}T*OTL.ghg" -
    exec cp {} "$TMP_DIR/" \;

# Redirect logs
export SLURM_OUT="${OUTPUT_DIR}/wavelet_${SLURM_ARRAY_JOB_ID}_${
    SLURM_ARRAY_TASK_ID}.out"
export SLURM_ERR="${OUTPUT_DIR}/wavelet_${SLURM_ARRAY_JOB_ID}_${
    SLURM_ARRAY_TASK_ID}.err"
exec >$SLURM_OUT 2>$SLURM_ERR

# Launch Python script
python wavelet_transform.py "$TMP_DIR" "${OUTPUT_DIR}/test_output.txt
    "
```

7 Bibliography

Anderson, D. E., Verma, S. B., & Rosenberg, N. J. (1984). Eddy correlation measurements of CO2, latent heat, and sensible heat fluxes over a crop surface. *Boundary-Layer Meteorology*, *29*(3), 263–272. https://doi.org/10.1007/BF00119792

Aubinet, M., Chermanne, B., Vandenhaute, M., Longdoz, B., Yernaux, M., & Laitat, E. (2001). Long term carbon dioxide exchange above a mixed forest in the belgian ardennes. *Agricultural and Forest Meteorology*, *108*(4), 293–315. https://doi.org/10.1016/S0168-1923(01)00244-1

Aubinet, M., Grelle, A., Ibrom, A., Rannik, Ü., Moncrieff, J., Foken, T., Kowalski, A., Martin, P., Berbigier, P., Bernhofer, C., Clement, R., Elbers, J., Granier, A., Grünwald, T., Morgenstern, K., Pilegaard, K., Rebmann, C., Snijders, W., Valentini, R., & Vesala, T. (1999). Estimates of the annual net carbon and water exchange of forests: The EUROFLUX methodology. In *Advances in ecological research* (pp. 113–175, Vol. 30). Elsevier. https://doi.org/10.1016/S0065-2504(08)60018-5

Aubinet, M., Vesala, T., & Papale, D. (Eds.). (2012). *Eddy covariance: A practical guide to measurement and data analysis*. Springer Netherlands. https://doi.org/10.1007/978-94-007-2351-1

Avissar, R., & Schmidt, T. (1998). An evaluation of the scale at which ground-surface heat flux patchiness affects the convective boundary layer using large-eddy simulations [Publisher: American Meteorological Society]. *Journal of the Atmospheric Sciences*, *55*(16), 2666–2689. https://doi.org/10.1175/1520-0469(1998)055<2666:aeotsa>2.0.co;2

Baldocchi, D. D. (2003). Assessing the eddy covariance technique for evaluating carbon dioxide exchange rates of ecosystems: Past, present and future. *Global Change Biology*, *9*(4), 479–492. https://doi.org/10.1046/j.1365-2486.2003.00629.x

Baldocchi, D. D., Hincks, B. B., & Meyers, T. P. (1988). Measuring biosphere□atmosphere exchanges of biologically related gases with micrometeorological methods. *Ecology*, *69*(5), 1331–1340. https://doi.org/10.2307/1941631

Barr, A., Morgenstern, K., Black, T., McCaughey, J., & Nesic, Z. (2006). Surface energy balance closure by the eddy-covariance method above three boreal forest stands and implications for the measurement of the CO2 flux. *Agricultural and Forest Meteorology*, *140*(1), 322–337. https://doi.org/10.1016/j.agrformet.2006.08.007

Bastida, F., García, C., Fierer, N., Eldridge, D. J., Bowker, M. A., Abades, S., Alfaro, F. D., Asefaw Berhe, A., Cutler, N. A., Gallardo, A., García-Velázquez, L., Hart, S. C., Hayes, P. E., Hernández, T., Hseu, Z.-Y., Jehmlich, N., Kirchmair, M., Lambers, H., Neuhauser, S., … Delgado-Baquerizo, M. (2019). Global ecological predictors of the soil priming effect. *Nature Communications*, *10*(1), 3481. https://doi.org/10.1038/s41467-019-11472-7

BE-lon ICOS ecosystem station labelling report (Labelling Report). (2017). Integrated Carbon Observation System (ICOS). https://meta.icos-cp.eu/objects/eo_cBxOeMONH2G8z4g0G_60J

BE-vie ICOS ecosystem station labelling report (Labelling Report). (2020). Integrated Carbon Observation System (ICOS). https://meta.icos-cp.eu/objects/xiiL_kyPVoN35ecLfEMOPrEV

Bernard, L., Basile□Doelsch, I., Derrien, D., Fanin, N., Fontaine, S., Guenet, B., Karimi, B., Marsden, C., & Maron, P.-A. (2022). Advancing the mechanistic understanding of the priming effect on soil organic matter mineralisation. *Functional Ecology*, *36*(6), 1355–1377. https://doi.org/10.1111/1365-2435.14038

Bitton, J. (2019). *Analyse multi-échelle de l'évolution des flux de chaleur sensible et latente échangés entre un écosystème forestier et l'atmosphère au moyen de la transformée en ondelettes continue* [Master's thesis]. University of Liège.

Brötz, B., Eigenmann, R., Dörnbrack, A., Foken, T., & Wirth, V. (2014). Early-morning flow transition in a valley in low-mountain terrain under clear-sky conditions. *Boundary-Layer Meteorology*, *152*(1), 45–63. https://doi.org/10.1007/s10546-014-9921-7

Charuchittipan, D., Babel, W., Mauder, M., Leps, J.-P., & Foken, T. (2014). Extension of the averaging time in eddy-covariance measurements and its effect on the energy balance closure. *Boundary-Layer Meteorology*, *152*(3), 303–327. https://doi.org/10.1007/s10546-014-9922-6

Collineau, S., & Brunet, Y. (1993a). Detection of turbulent coherent motions in a forest canopy part i: Wavelet analysis. *Boundary-Layer Meteorology*, *65*(4), 357–379. https://doi.org/10.1007/BF00707033

Collineau, S., & Brunet, Y. (1993b). Detection of turbulent coherent motions in a forest canopy part II: Time-scales and conditional averages. *Boundary-Layer Meteorology*, *66*(1), 49–73. https://doi.org/10.1007/BF00705459

Daubechies, I. (1990). The wavelet transform, time-frequency localization and signal analysis. *IEEE Transactions on Information Theory*, *36*(5), 961–1005. https://doi.org/10.1109/18.57199

Desjardins, R., Macpherson, J., Neumann, H., Den Hartog, G., & Schuepp, P. (1995). Flux estimates of latent and sensible heat, carbon dioxide, and ozone using an aircraft-tower combination. *Atmospheric Environment*, *29*(21), 3147–3158. https://doi.org/10.1016/1352-2310(95)00007-L

Destouet, G., Besic, N., Joetzjer, E., & Cuntz, M. (2024, November 15). Turbulent transport extraction in time and frequency and the estimation of eddy fluxes at high resolution. https://doi.org/10.5194/egusphere-2024-3243

Dupont, S., Irvine, M. R., & Bidot, C. (2024). Morning transition of the coupled vegetation canopy and atmospheric boundary layer turbulence according to the wind intensity. *Journal of the Atmospheric Sciences*, *81*(7), 1225–1249. https://doi.org/10.1175/JAS-D-23-0201.1

Eigenmann, R., Kalthoff, N., Foken, T., Dorninger, M., Kohler, M., Legain, D., Pigeon, G., Piguet, B., Schüttemeyer, D., & Traulle, O. (2011). Surface energy balance and turbulence network during the convective and orographically□induced precipitation study (COPS). *Quarterly Journal of the Royal Meteorological Society*, *137*, 57–69. https://doi.org/10.1002/qj.704

Etling, D., & Brown, R. A. (1993). Roll vortices in the planetary boundary layer: A review [Publisher: Springer Science and Business Media LLC]. *Boundary-Layer Meteorology*, *65*(3), 215–248. https://doi.org/10.1007/bf00705527

Falge, E., Baldocchi, D., Olson, R., Anthoni, P., Aubinet, M., Bernhofer, C., Burba, G., Ceulemans, R., Clement, R., Dolman, H., Granier, A., Gross, P., Grünwald, T., Hollinger, D., Jensen, N.-O., Katul, G., Keronen, P., Kowalski, A., Lai, C. T., … Wofsy, S. (2001). Gap filling strategies for defensible annual sums of net ecosystem exchange. *Agricultural and Forest Meteorology*, *107*(1), 43–69. https://doi.org/10.1016/S0168-1923(00)00225-2

Fan, L., Zhang, F., Fan, H., & Zhang, C. (2019). Brief review of image denoising techniques. *Visual Computing for Industry, Biomedicine, and Art*, *2*(1), 7. https://doi.org/10.1186/s42492-019-0016-7

Farge, M. (1992). WAVELET TRANSFORMS AND THEIR APPLICATIONS TO TURBULENCE. *Annual Review of Fluid Mechanics*, *24*(1), 395–458. https://doi.org/10.1146/annurev.fl.24.010192.002143

Finnigan, J. J., Clement, R., Malhi, Y., Leuning, R., & Cleugh, H. (2003). A re-evaluation of long-term flux measurement techniques part i: Averaging and coordinate rotation. *Boundary-Layer Meteorology*, *107*(1), 1–48. https://doi.org/10.1023/A:1021554900225

Foken, T., Wimmer, F., Mauder, M., Thomas, C., & Liebethal, C. (2006). Some aspects of the energy balance closure problem. *Atmospheric Chemistry and Physics*, *6*(12), 4395–4402. https://doi.org/10.5194/acp-6-4395-2006

Foken, T., Foken, T., & Nappo, C. J. (2008). *Micrometeorology*. Springer.

Foken, T., & Wichura, B. (1996). Tools for quality assessment of surface-based flux measurements. *Agricultural and Forest Meteorology*, *78*(1), 83–105. https://doi.org/10.1016/0168-1923(95)02248-1

Foken, T. (2008). THE ENERGY BALANCE CLOSURE PROBLEM: AN OVERVIEW. *Ecological Applications*, *18*(6), 1351–1367. https://doi.org/10.1890/06-0922.1

Foken, T., & Nappo, C. J. (2008). *Micrometeorology*. Springer.

Franssen, H. H., Stöckli, R., Lehner, I., Rotenberg, E., & Seneviratne, S. (2010). Energy balance closure of eddy-covariance data: A multisite analysis for european FLUXNET stations. *Agricultural and Forest Meteorology*, *150*(12), 1553–1567. https://doi.org/10.1016/j.agrformet.2010.08.005

Gao, W., Shaw, R. H., & Paw U, K. T. (1989). Observation of organized structure in turbulent flow within and above a forest canopy. *Boundary-Layer Meteorology*, *47*(1), 349–377. https://doi.org/10.1007/BF00122339

Goulden, M. L., Daube, B. C., Fan, S.-M., Sutton, D. J., Bazzaz, A., Munger, J. W., & Wofsy, S. C. (1997). Physiological responses of a black spruce forest to weather. *Journal of Geophysical Research: Atmospheres*, *102*, 28987–28996. https://doi.org/10.1029/97JD01111

Grossmann, A., & Morlet, J. (1984). Decomposition of hardy functions into square integrable wavelets of constant shape [_eprint: https://doi.org/10.1137/0515056]. *SIAM Journal on Mathematical Analysis*, *15*(4), 723–736. https://doi.org/10.1137/0515056

Gu, L., Meyers, T., Pallardy, S. G., Hanson, P. J., Yang, B., Heuer, M., Hosman, K. P., Liu, Q., Riggs, J. S., Sluss, D., & Wullschleger, S. D. (2007). Influences of biomass heat and biochemical energy storages on the land surface fluxes and radiative temperature. *Journal of Geophysical Research: Atmospheres*, *112*, 2006JD007425. https://doi.org/10.1029/2006JD007425

Högström, U. (1988). Non-dimensional wind and temperature profiles in the atmospheric surface layer: A re-evaluation. *Boundary-Layer Meteorology*, *42*(1), 55–78. https://doi.org/10.1007/BF00119875

Högström, U., Bergström, H., Smedman, A.-S., Halldin, S., & Lindroth, A. (1989). Turbulent exchange above a pine forest, i: Fluxes and gradients. *Boundary-Layer Meteorology*, *49*(1), 197–217. https://doi.org/10.1007/BF00116411

Högström, U., Hunt, J. C. R., & Smedman, A.-S. (2002). Theory and measurements for turbulence spectra and variances in the atmospheric neutral surface layer. *Boundary-Layer Meteorology*, *103*(1), 101–124. https://doi.org/10.1023/A:1014579828712

Inagaki, A., Letzel, M. O., Raasch, S., & Kanda, M. (2006). Impact of surface heterogeneity on energy imbalance: A study using LES [Publisher: Meteorological Society of Japan]. *Journal of the Meteorological Society of Japan. Ser. II*, *84*(1), 187–198. https://doi.org/10.2151/jmsj.84.187

Jarvis, P. G., Massheder, J. M., Hale, S. E., Moncrieff, J. B., Rayment, M., & Scott, S. L. (1997). Seasonal variation of carbon dioxide, water vapor, and energy exchanges of a boreal black spruce forest. *Journal of Geophysical Research: Atmospheres*, *102*, 28953–28966. https://doi.org/10.1029/97JD01176

Kaimal, J. C., & Finnigan, J. J. (1994, March 10). *Atmospheric boundary layer flows: Their structure and measurement*. Oxford University Press. https://doi.org/10.1093/oso/9780195062397.001.0001

Kanda, M., Inagaki, A., Letzel, M. O., Raasch, S., & Watanabe, T. (2004). LES study of the energy imbalance problem with eddy covariance fluxes [Publisher: Springer Science and Business Media LLC]. *Boundary-Layer Meteorology*, *110*(3), 381–404. https://doi.org/10.1023/b:boun.0000007225.45548.7a

Katul, G., & Vidakovic, B. (1996). The partitioning of attached and detached eddy motion in the atmospheric surface layer using lorentz wavelet filtering. *Boundary-Layer Meteorology*, *77*(2), 153–172. https://doi.org/10.1007/BF00119576

Katul, G. G., Geron, C. D., Hsieh, C.-I., Vidakovic, B., & Guenther, A. B. (1998). Active turbulence and scalar transport near the forest–atmosphere interface. *Journal of Applied Meteorology*, *37*(12), 1533–1546. https://doi.org/10.1175/1520-0450(1998)037<1533:ATASTN>2.0.CO;2

Kirby, J. F., & Swain, C. J. (2013). Power spectral estimates using two-dimensional morlet-fan wavelets with emphasis on the long wavelengths: Jackknife errors, bandwidth resolution and orthogonality properties. *Geophysical Journal International*, *194*(1), 78–99. https://doi.org/10.1093/gji/ggt103

Kljun, N., Calanca, P., Rotach, M. W., & Schmid, H. P. (2015). A simple two-dimensional parameterisation for flux footprint prediction (FFP). *Geoscientific Model Development*, *8*(11), 3695–3713. https://doi.org/10.5194/gmd-8-3695-2015

Kumar, P., & Foufoula□Georgiou, E. (1997). Wavelet analysis for geophysical applications. *Reviews of Geophysics*, *35*(4), 385–412. https://doi.org/10.1029/97RG00427

Lee, X. (1998). On micrometeorological observations of surface-air exchange over tall vegetation [Publisher: Elsevier BV]. *Agricultural and Forest Meteorology*, *91*(1), 39–49. https://doi.org/10.1016/s0168-1923(98)00071-9

Lee, X., & Black, T. A. (1993). Atmospheric turbulence within and above a douglas-fir stand. part II: Eddy fluxes of sensible heat and water vapour [Publisher: Springer Science and Business Media LLC]. *Boundary-Layer Meteorology*, *64*(4), 369–389. https://doi.org/10.1007/bf00711706

Lee, X., Massman, W., & Law, B. (Eds.). (2005). *Handbook of micrometeorology* (Vol. 29). Springer Netherlands. https://doi.org/10.1007/1-4020-2265-4

Letzel, M. O., & Raasch, S. (2003). Large eddy simulation of thermally induced oscillations in the convective boundary layer. *Journal of the Atmospheric Sciences*, *60*(18), 2328–2341. https://doi.org/10.1175/1520-0469(2003)060<2328:LESOTI>2.0.CO;2

Li, D., & Bou-Zeid, E. (2011). Coherent structures and the dissimilarity of turbulent transport of momentum and scalars in the unstable atmospheric surface layer. *Boundary-Layer Meteorology*, *140*(2), 243–262. https://doi.org/10.1007/s10546-011-9613-5

Li, Y., Wu, Y., Tang, J., Zhu, P., Gao, Z., & Yang, Y. (2023). Quantitative evaluation of wavelet analysis method for turbulent flux calculation of non□stationary series. *Geophysical Research Letters*, *50*(5), e2022GL101591. https://doi.org/10.1029/2022GL101591

Liu, H., Liu, C., Huang, J., Desai, A. R., Zhang, Q., Ghannam, K., & Katul, G. G. (2024). Scalar flux profiles in the unstable atmospheric surface layer under the influence of large eddies: Implications for eddy covariance flux measurements and the non□closure problem. *Geophysical Research Letters*, *51*(1), e2023GL106649. https://doi.org/10.1029/2023GL106649

Liu, Z.-Q. (1991). Scale space approach to directional analysis of images. *Applied Optics*, *30*(11), 1369. https://doi.org/10.1364/AO.30.001369

Lloyd, J., & Taylor, J. A. (1994). On the temperature dependence of soil respiration. *Functional Ecology*, *8*(3), 315. https://doi.org/10.2307/2389824

Loescher, H. W., Law, B. E., Mahrt, L., Hollinger, D. Y., Campbell, J., & Wofsy, S. C. (2006). Uncertainties in, and interpretation of, carbon flux estimates using the eddy covariance technique. *Journal of Geophysical Research: Atmospheres*, *111*, 2005JD006932. https://doi.org/10.1029/2005JD006932

Mahrt, L. (1998). Flux sampling errors for aircraft and towers. *Journal of Atmospheric and Oceanic Technology*, *15*(2), 416–429. https://doi.org/10.1175/1520-0426(1998)015<0416:FSEFAA>2.0.CO;2

Mauder, M., Desjardins, R. L., & MacPherson, I. (2007a). Scale analysis of airborne flux measurements over heterogeneous terrain in a boreal ecosystem [Publisher: American Geophysical Union (AGU)]. *Journal of Geophysical Research: Atmospheres*, *112*. https://doi.org/10.1029/2006jd008133

Mauder, M., Desjardins, R. L., & MacPherson, I. (2007b). Scale analysis of airborne flux measurements over heterogeneous terrain in a boreal ecosystem. *Journal of Geophysical Research: Atmospheres*, *112*, 2006JD008133. https://doi.org/10.1029/2006JD008133

Mauder, M., Desjardins, R. L., Pattey, E., & Worth, D. (2010). An attempt to close the daytime surface energy balance using spatially-averaged flux measurements. *Boundary-Layer Meteorology*, *136*(2), 175–191. https://doi.org/10.1007/s10546-010-9497-9

Mauder, M., & Foken, T. (2006). Impact of post-field data processing on eddy covariance flux estimates and energy balance closure [Publisher: Schweizerbart]. *Meteorologische Zeitschrift*, *15*(6), 597–609. https://doi.org/10.1127/0941-2948/2006/0167

Mauder, M., Foken, T., & Cuxart, J. (2020). Surface-energy-balance closure over land: A review. *Boundary-Layer Meteorology*, *177*(2), 395–426. https://doi.org/10.1007/s10546-020-00529-6

Meyers, T. (2004a). An assessment of storage terms in the surface energy balance of maize and soybean. *Agricultural and Forest Meteorology*, *125*(1), 105–115. https://doi.org/10.1016/j.agrformet.2004.03.001

Meyers, T. (2004b). An assessment of storage terms in the surface energy balance of maize and soybean. *Agricultural and Forest Meteorology*, *125*(1), 105–115. https://doi.org/10.1016/j.agrformet.2004.03.001

Nobach, H., Tropea, C., Cordier, L., Bonnet, J.-P., Delville, J., Lewalle, J., Farge, M., Schneider, K., & Adrian, R. (2007). Review of some fundamentals of data processing. In C. Tropea, A. L. Yarin, & J. F. Foss (Eds.), *Springer handbook of experimental fluid mechanics* (pp. 1337–1398). Springer Berlin Heidelberg. https://doi.org/10.1007/978-3-540-30299-5_22

Oncley, S. P., Foken, T., Vogt, R., Kohsiek, W., DeBruin, H. A. R., Bernhofer, C., Christen, A., Gorsel, E. V., Grantz, D., Feigenwinter, C., Lehner, I., Liebethal, C., Liu, H., Mauder, M., Pitacco, A., Ribeiro, L., & Weidinger, T. (2007). The energy balance experiment EBEX-2000. part i: Overview and energy balance. *Boundary-Layer Meteorology*, *123*(1), 1–28. https://doi.org/10.1007/s10546-007-9161-1

Panin, G. N., Tetzlaff, G., & Raabe, A. (1998). Inhomogeneity of the land surface and problems in theParameterization of surface fluxes in natural conditions. *Theoretical and Applied Climatology*, *60*(1), 163–178. https://doi.org/10.1007/s007040050041

Patton, E. G., Sullivan, P. P., & Moeng, C.-H. (2005). The influence of idealized heterogeneity on wet and dry planetary boundary layers coupled to the land surface [Publisher: American Meteorological Society]. *Journal of the Atmospheric Sciences*, *62*(7), 2078–2097. https://doi.org/10.1175/jas3465.1

Patton, E. G., Sullivan, P. P., Shaw, R. H., Finnigan, J. J., & Weil, J. C. (2016). Atmospheric stability influences on coupled boundary layer and canopy turbulence. *Journal of the Atmospheric Sciences*, *73*(4), 1621–1647. https://doi.org/10.1175/JAS-D-15-0068.1

Raupach, M. R., Finnigan, J. J., & Brunei, Y. (1996). Coherent eddies and turbulence in vegetation canopies: The mixing-layer analogy. *Boundary-Layer Meteorology*, *78*(3), 351–382. https://doi.org/10.1007/BF00120941

Reichstein, M., Rey, A., Freibauer, A., Tenhunen, J., Valentini, R., Banza, J., Casals, P., Cheng, Y., Grünzweig, J. M., Irvine, J., Joffre, R., Law, B. E., Loustau, D., Miglietta, F., Oechel, W., Ourcival, J.-M., Pereira, J. S., Peressotti, A., Ponti, F., … Yakir, D. (2003). Modeling temporal and large□scale spatial variability of soil respiration from soil water availability, temperature and vegetation productivity indices. *Global Biogeochemical Cycles*, *17*(4), 2003GB002035. https://doi.org/10.1029/2003GB002035

Rendón, A. M., Salazar, J. F., Palacio, C. A., & Wirth, V. (2015). Temperature inversion breakup with impacts on air quality in urban valleys influenced by topographic shading. *Journal of Applied Meteorology and Climatology*, *54*(2), 302–321. https://doi.org/10.1175/JAMC-D-14-0111.1

Scanlon, T. M., & Sahu, P. (2008). On the correlation structure of water vapor and carbon dioxide in the atmospheric surface layer: A basis for flux partitioning. *Water Resources Research*, *44*(10), 2008WR006932. https://doi.org/10.1029/2008WR006932

Schaller, C., Göckede, M., & Foken, T. (2017). Flux calculation of short turbulent events – comparison of three methods. *Atmospheric Measurement Techniques*, *10*(3), 869–880. https://doi.org/10.5194/amt-10-869-2017

Stoy, P. C., Mauder, M., Foken, T., Marcolla, B., Boegh, E., Ibrom, A., Arain, M. A., Arneth, A., Aurela, M., Bernhofer, C., Cescatti, A., Dellwik, E., Duce, P., Gianelle, D., Van Gorsel, E., Kiely, G., Knohl, A., Margolis, H., McCaughey, H., … Varlagin, A. (2013). A data-driven analysis of energy balance closure across FLUXNET research sites: The role of landscape scale heterogeneity. *Agricultural and Forest Meteorology*, *171-172*, 137–152. https://doi.org/10.1016/j.agrformet.2012.11.004

Stull, R. B. (2003). *An introduction to boundary layer meteorology* (Reprint). Kluwer.

Sühring, M., & Raasch, S. (2013). Heterogeneity-induced heat-flux patterns in the convective boundary layer: Can they be detected from observations and is there a blending height?—a large-eddy simulation study for the LITFASS-2003 experiment. *Boundary-Layer Meteorology*, *148*(2), 309–331. https://doi.org/10.1007/s10546-013-9822-1

Sun, J., Desjardins, R., Mahrt, L., & MacPherson, I. (1998). Transport of carbon dioxide, water vapor, and ozone by turbulence and local circulations. *Journal of Geophysical Research: Atmospheres*, *103*, 25873–25885. https://doi.org/10.1029/98JD02439

Terradellas, E., Morales, G., Cuxart, J., & Yagüe, C. (2001). Wavelet methods: Application to the study of the stable atmospheric boundary layer under non-stationary conditions. *Dynamics of Atmospheres and Oceans*, *34*(2), 225–244. https://doi.org/10.1016/S0377-0265(01)00069-0

Thomas, C., & Foken, T. (2005). Detection of long-term coherent exchange over spruce forest using wavelet analysis. *Theoretical and Applied Climatology*, *80*(2), 91–104. https://doi.org/10.1007/s00704-004-0093-0

Thomas, C., & Foken, T. (2007). Flux contribution of coherent structures and its implications for the exchange of energy and matter in a tall spruce canopy. *Boundary-Layer Meteorology*, *123*(2), 317–337. https://doi.org/10.1007/s10546-006-9144-7

Torrence, C., & Compo, G. P. (1998). A practical guide to wavelet analysis. *Bulletin of the American Meteorological Society*, *79*(1), 61–78. https://doi.org/10.1175/1520-0477(1998)079<0061:APGTWA>2.0.CO;2

Turnipseed, A., Blanken, P., Anderson, D., & Monson, R. (2002). Energy budget above a high-elevation subalpine forest in complex topography. *Agricultural and Forest Meteorology*, *110*(3), 177–201. https://doi.org/10.1016/S0168-1923(01)00290-8

Turnipseed, A. A., Anderson, D. E., Burns, S., Blanken, P. D., & Monson, R. K. (2004). Airflows and turbulent flux measurements in mountainous terrain. *Agricultural and Forest Meteorology*, *125*(3), 187–205. https://doi.org/10.1016/j.agrformet.2004.04.007

Twine, T., Kustas, W., Norman, J., Cook, D., Houser, P., Meyers, T., Prueger, J., Starks, P., & Wesely, M. (2000). Correcting eddy-covariance flux underestimates over a grassland. *Agricultural and Forest Meteorology*, *103*(3), 279–300. https://doi.org/10.1016/S0168-1923(00)00123-4

Tzvetkov, D. (2023). *Analysis of turbulent fluxes with the means of the continuous wavelet transform on the belgian ICOS sites of lonzée and vielsalm* [Master's thesis]. University of Liège.

Ueyama, M., Hirata, R., Mano, M., Hamotani, K., Harazono, Y., Hirano, T., Miyata, A., Takagi, K., & Takahashi, Y. (2012). Influences of various calculation options on heat, water and carbon fluxes determined by open- and closed-path eddy covariance methods. *Tellus B: Chemical and Physical Meteorology*, *64*(1), 19048. https://doi.org/10.3402/tellusb.v64i0.19048

Vidale, P. L., Pielke, R. A., Steyaert, L. T., & Barr, A. (1997). Case study modeling of turbulent and mesoscale fluxes over the BOREAS region. *Journal of Geophysical Research: Atmospheres*, *102*, 29167–29188. https://doi.org/10.1029/97JD02561

Vitale, D., Fratini, G., Bilancia, M., Nicolini, G., Sabbatini, S., & Papale, D. (2020). A robust data cleaning procedure for eddy covariance flux measurements. *Biogeosciences*, *17*(6), 1367–1391. https://doi.org/10.5194/bg-17-1367-2020

Wilson, K., Goldstein, A., Falge, E., Aubinet, M., Baldocchi, D., Berbigier, P., Bernhofer, C., Ceulemans, R., Dolman, H., Field, C., Grelle, A., Ibrom, A., Law, B., Kowalski, A., Meyers, T., Moncrieff, J., Monson, R., Oechel, W., Tenhunen, J., … Verma, S. (2002). Energy balance closure at FLUXNET sites. *Agricultural and Forest Meteorology*, *113*(1), 223–243. https://doi.org/10.1016/S0168-1923(02)00109-0

Zhang, F., Wei, J., Zhang, M., Bowman, K. P., Pan, L. L., Atlas, E., & Wofsy, S. C. (2015). Aircraft measurements of gravity waves in the upper troposphere and lower stratosphere during the START08 field experiment. *Atmospheric Chemistry and Physics*, *15*(13), 7667–7684. https://doi.org/10.5194/acp-15-7667-2015

Zhang, Y., Liu, H., Foken, T., Williams, Q. L., Mauder, M., & Thomas, C. (2011). Coherent structures and flux contribution over an inhomogeneously irrigated cotton field [Publisher: Springer Science and Business Media LLC]. *Theoretical and Applied Climatology*, *103*(1), 119–131. https://doi.org/10.1007/s00704-010-0287-6

Zhou, Y., Liu, H., Sühring, M., & Li, X. (2024). Implications of energy balance non-closure on carbon dioxide flux uncertainties: Insights from large eddy simulations in convective boundary layers [Publisher: Elsevier BV]. *Agricultural and Forest Meteorology*, *358*, 110211. https://doi.org/10.1016/j.agrformet.2024.110211